THESIS

IMPROVEMENTS IN THIN FILM CdTe BACK CONTACT AND INTERFACE LAYERS

THROUGH SPUTTER DEPOSITION OF METALS AND SEMICONDUCTOR MATERIALS

Submitted by

Anna Kindvall

Department of Mechanical Engineering

In partial fulfillment of the requirements

For the Degree of Master of Science

Colorado State University

Fort Collins, Colorado

Fall 2019

Master's Committee:

   Advisor: Walajabad Sampath

   Jason Kephart
   Jose de la Venta

ABSTRACT

IMPROVEMENTS IN THIN FILM CdTe BACK CONTACT AND INTERFACE LAYERS
THROUGH SPUTTER DEPOSITION OF METALS AND SEMICONDUCTOR MATERIALS

The photovoltaic industry has grown at an average annual rate of 50% over the last ten years. In that time, solar module prices have dropped significantly, with the current levelized cost of electricity averaged at $0.03 per kilowatt hour. Cadmium telluride (CdTe) photovoltaics are a common commercially produced thin-film solar cell. The leader in CdTe module production and research and development is First Solar. First Solar has set the record for research scale CdTe devices, achieving an efficiency of 22.1%, far from the theoretical limit. Improving interface layers has been identified as one of the key strategies towards further improving device performance.

The focus of this study is on back contact interface layers. This research explores sputtered molybdenum oxide (MoO_x) and molybdenum nitride (MoN_x) thin films as alternative back contact to carbon and nickel paint in a polymer binder. The MoO_x and MoN_x films were characterized using resistivity measurements, Hall measurements to determine carrier concentrations, x-ray photoelectron spectroscopy to determine nitrogen and oxygen incorporation into the film and x-ray diffraction to determine crystallinity. Devices were fabricated using different compositions of molybdenum, molybdenum oxide, and molybdenum nitride with an aluminum capping layer as back contacts. This structure resulted in performances very similar to the baseline with carbon and nickel paint, proving it to be a viable alternative.

Additionally, this research study explored the option of zinc telluride (ZnTe) as a buffer layer between the CdTe and metal back contact. Copper doping assists in the CdTe device performance, however too much copper can be detrimental to device performance. The ZnTe layer allows for better valence band alignment and limits copper diffusion. The device structure with ZnTe resulted in a 17.6% device, which is comparable to the baseline structure. Early results indicated devices with ZnTe were more stable and robust over time.

ACKNOWLEDGEMENTS

TABLE OF CONTENTS

LIST OF TABLES

LIST OF FIGURES

1   INTRODUCTION

1.1 World Energy Demand

From 2010 to 2030 there is a predicted global energy usage increase of 39% [1]. Energy resources are limited and as of 2015, the world energy use was 18.5 TWy/y (Terawatt-years per year) [2]. Figure 1 displays the finite resources (coal, petroleum, natural gas, etc.) available as well as the renewable resources (wind, hydro, biomass, solar, etc.) available. Renewable energy can be defined as a natural energy source that is not depleted when used. Often renewable energy is referred to as clean energy.
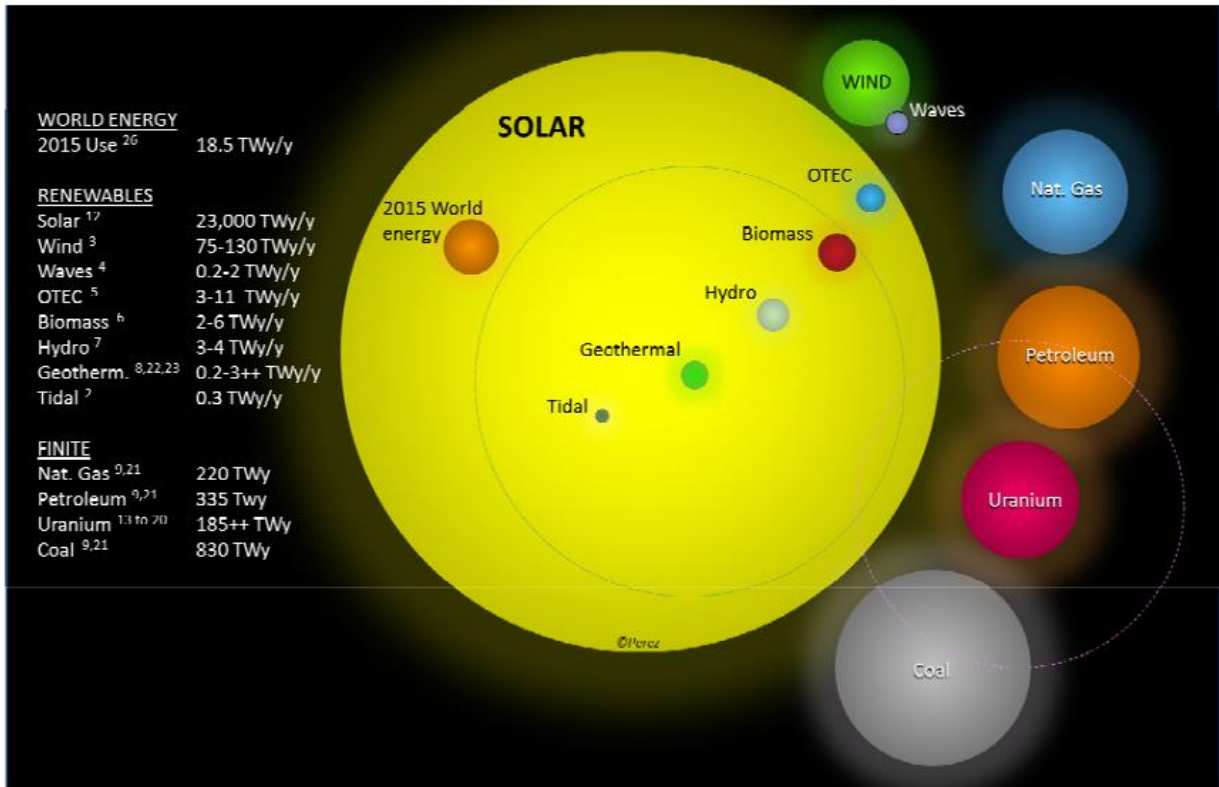
Figure 1: Estimate of world energy usage with finite and renewable energy sources as of 2015. Figure modified from [2].

Renewable energy production has an average annual growth rate of 2% of total energy supply in the world. Solar photovoltaics (PV) accounts for 37% of the renewable energy growth annually from 1990 to 2016 [3].
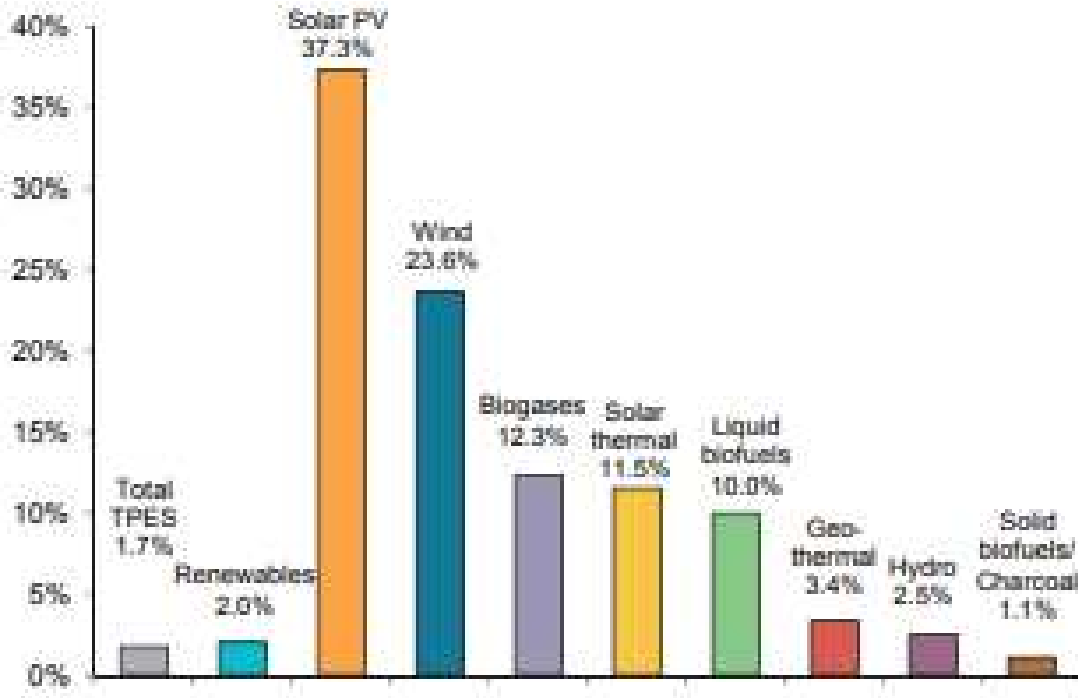
Figure 2: Renewable energy supply average annual growth from 1990 to 2016. Figure modified from [3].

Renewable energy sources are becoming more popular primarily due to the ability to mitigate greenhouse gases [4]. Sources of renewable energy include solar photovoltaics, concentrated solar power (CSP), wind energy, hydropower, biomass energy, geothermal energy and many others.

1.2 Solar Energy Background

1.2.1 History

The concept of using sunlight for energy has been around for centuries. The earliest accounts of using mirrors and magnifying glasses to start fires date back to 700 B.C. However, major advances in photovoltaic technologies are more recent in historical events. The

photovoltaic effect was discovered in 1839 by Edmond Becquerel, a French scientist. However, the first notable solar cell wasn't created until 1954 by Bell Telephone Laboratories. With their silicon solar cell, they achieved a 4% efficient cell. From that point, photovoltaic technology grew rapidly. The 1973 oil embargo changed the view of PV from space applications to terrestrial applications [5]. By the end of the twentieth century (1999) there were 1000 megawatts of installed solar capacity [6]. As of 2017, the total world capacity of installed solar was 390,625 megawatts [7].

Each type of solar energy record produced from 1975 to present day has been tracked by NREL. First Solar is currently the record holder for CdTe research scale solar cells with a 22.1 % efficient cell. Records for thin-film solar, silicon, multijunction and more are displayed in Figure 8 at the end of the chapter.

1.2.2 Cost and Market

Photovoltaic costs have dropped significantly over the past decades. In a cost comparison of residential PV systems from 2010 to 2018, there was an overall reduction of 63%. Module expenses dropped 82%, labor costs dropped 77%, and there was a 57% reduction in hardware expenses from 2010-2018 [8]. The cost decreases for residential PV can be attributed to higher module efficiency, higher productivity labor, lower permitting cost, and many other factors.

As with the commercial PV systems, there was an overall cost reduction of 66% from 2010 to 2018. Hardware costs were reduced by 79%, module expenses dropped 82%, and labor costs dropped 50% from 2010-2018 [8].The major price decreases in commercial PV systems can be credited to lower inverter price, lower permitting and interconnection cost, and higher module efficiencies. Solar photovoltaics are competitive in today's energy market on an unsubsidized level.

1.2.3   Solar Potential

There are many stars in solar system, one of which happens to be the sun. The sun produces very large quantities of energy, and 95% of the energy output is light. The sun has a power output of 3.86×10^{20} Megawatts (MW) per second [9]. The sunlight that reaches earth's surface is generally reduced by about 30% through the atmosphere [10]. While the sunlight reaching the Earth's surface is reduced, the sun still produces enough energy in one hour to power the world for a year [11].

1.3   Photovoltaic Fundamentals

1.3.1   Photovoltaics

Starting at the smallest level, everything is made up of atoms. Each atom has a core (nucleus) with protons (positively charged) and neutrons (neutral). Electrons (negatively charged) revolve around the core in energy orbitals. Each element's atomic number corresponds to the number of protons and electrons it has. Each atom has a set number of electron shells which hold a certain number of electrons. Valence electrons are the electrons in which have higher energy and are in the farthest shell from the atom's nucleus. The outer shell is called the valence shell or the valence band [12].

All materials are formed from atoms. The electrical properties from the atoms impact the type of material formed. Materials fall into one of three categories: conductors, insulators, or semiconductors.

Conducing materials are able to easily conduct electrical current and have very low resistivity. Common conducting elements are metals such as copper and aluminum. These metals conduct electricity due to having one valence electron that is loosely bound. The valence

electron with a little bit of energy, can become a free electron that can easily carry current through a material.

Insulating materials are very resistive materials and do not conduct electrical current. Insulating materials are often material compounds include glass and plastics. Insulating material atoms have tightly bound valence electrons.

Semiconductors are not conductors or insulators, semiconductors are somewhere in-between in terms of electrical conductivity. Semiconductors can be single elements or compounds. Examples of both are silicon and cadmium telluride (CdTe).

1.3.2   Semiconductors

The valence band is the outer most shell of the atom that still contains electrons. If the electron gains energy, it can become a free electron and exist in the conduction band. In the realm of photovoltaics, the electron gains energy to jump into the conduction band from sunlight (photons).
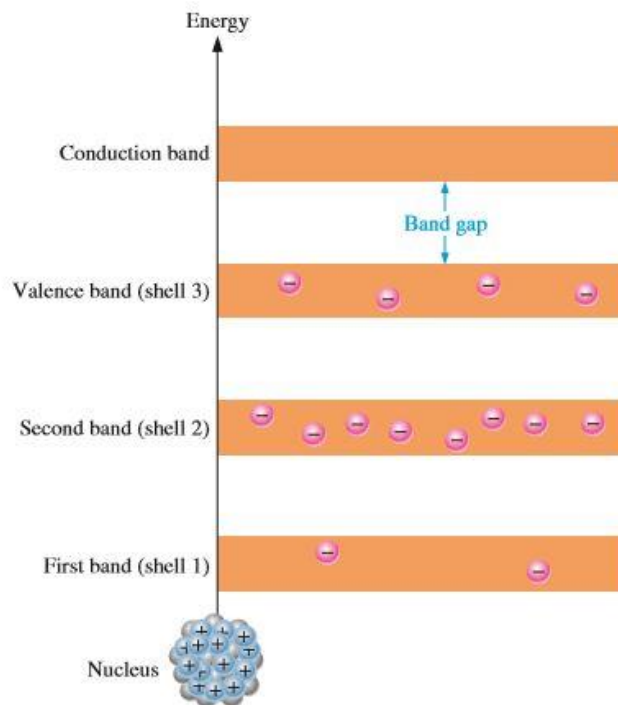
Figure 3: Example band diagram of intrinsic silicon. Referenced from [12].

The energy difference between the valence band and the conduction band is the bandgap (EG). In semiconductors, the Fermi level is an energy level found between the bandgap. The Fermi level (E_F) is an energy level where states have a 50% probability of being occupied with an electron [13]. The vacuum level (E_{VAC}) can be defined as the energy level of an electron positioned at rest outside of the sample surface. Many measurements are performed using the vacuum level as a reference. The ionization energy (IE) is a measurement between the valence band maximum to the vacuum level. The electron affinity (EA) is a measurement of how much energy is needed to move an electron from the conduction band to the vacuum level [14]. The work function (WF) is a measurement of how much energy it takes to move an electron from the Fermi level to the vacuum level [14]. Defined terms can be visualized in Figure 4.

6
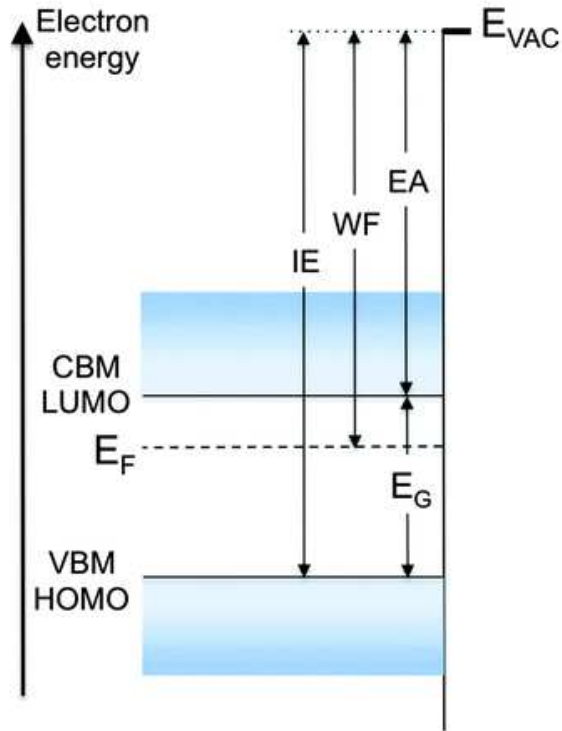
Figure 4: Energy diagram of a semiconductor. Referenced from [15].

Typically, semiconductors are resistive. Often semiconductors need to be doped in order to increase current carriers. Doping can be done by adding extra electrons making the material n-type or by adding extra holes (missing electrons) to make the material p-type. Often this is done by doping the material with another element that has an extra electron or has an extra hole as seen in Figure 5.
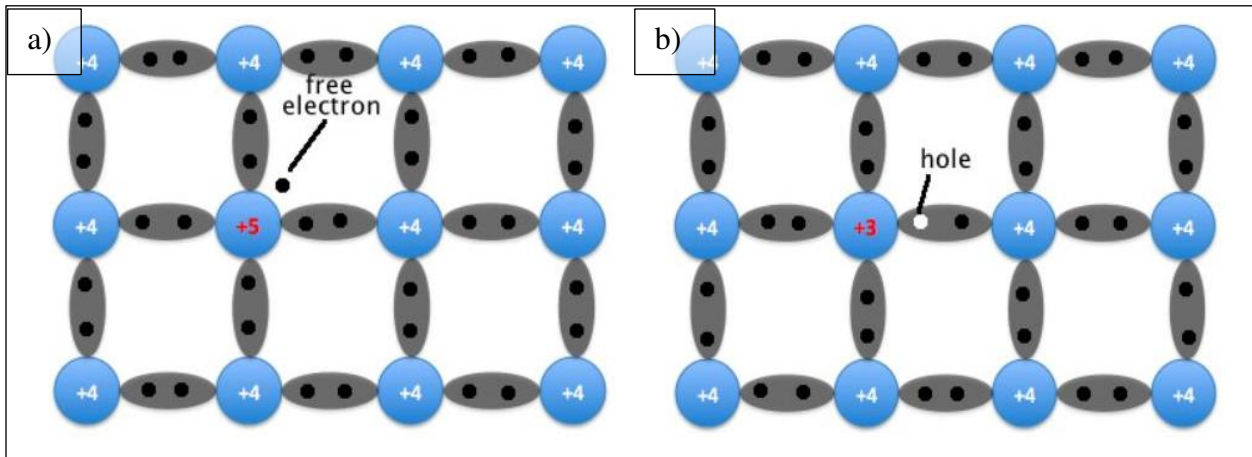
Figure 5: a) N-type material with a free electron in the crystal structure. b) P-type material with a hole in the crystal structure. Images referenced from [16].

The boundary between the n-type and p-type semiconducting materials is called the PN junction [12]. The depletion region or space charge region is formed when free electrons and holes diffuse across the junction causing a depletion of charge carriers [12]. When in equilibrium, the Fermi level between the n-type and p-type materials must be flat. The region outside the space charge region is called the quasi-neutral region where the bands are flat.

1.3.3   Shockley Queisser Limit

The Shockley Queisser Limit is a limit of maximum power conversion in solar cell materials as seen in Figure 7.

There are four main assumptions within the Shockley-Queisser Limit at its simplest form. Those assumptions must be understood and followed for the following to be true. The first assumption is that for all photon energies greater than the band gap, the probability of absorption in the material is unity. For all photon energies less than the band gap, there is zero probability of generating an electron-hole pair. The second assumption is charge carriers thermalize at the band edges. The third assumption is for all photogenerated electron- hole pairs, the collection probability at short circuit is unity. The fourth and final assumption is the only loss mechanism is

8

radiative recombination of electron-hole pairs except for the photons not absorbed in the first assumption and the losses from the second assumption dealing with thermalization.

1.3.4   Solar Spectrum

The sunlight that reaches the Earth has different energies. Each particle or wave is called a photon. The photons have different energies and wavelengths. The energy of a photon (E) can be described by the following equation.

$$E = \frac{hc}{\lambda} \tag{1}$$

Where h is Plank's constant, c is the speed of light, and λ is wavelength of light.

A common term for discussing the spectral distribution of sunlight is air mass. Air mass zero radiation (AM0) is the amount of radiant power per unit area which is perpendicular to the sun. AM0 is calculated outside of the earth's atmosphere. Air mass one radiation (AM1) is the radiation when the sun is directly overhead [10]. Much of the solar spectrum is direct radiation however there is a portion of absorbed light that can be attributed to indirect radiation or diffuse radiation. The general standard for testing photovoltaic modules or cells is AM1.5 and an averaged total power density of 1kW/m^2 [17]. The ASTM G173-03 standard solar spectrum is shown in Figure 6.

ASTM G173-03 Reference Spectra
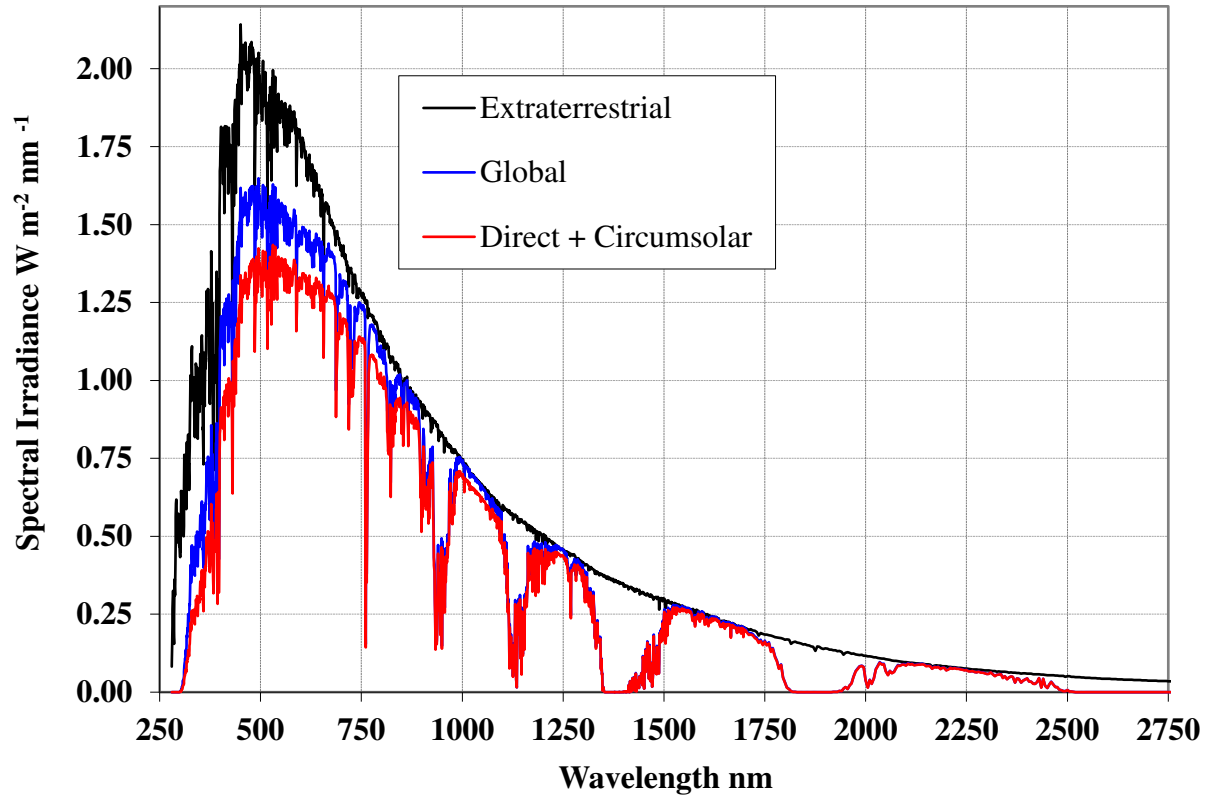
Figure 6: Solar spectrum reference for AM1.5 following ASTM G173-03. Data from [18].

1.3.5 CdTe Photovoltaics

There are many advantages to CdTe photovoltaics as compared to other PV technologies. CdTe technology has one of the lowest manufacturing costs [19]. CdTe also has an ideal band gap, aligning very well with the solar spectrum for better photon absorption [20]. Figure 7 shows detailed balance efficiency limits considering AM 1.5.
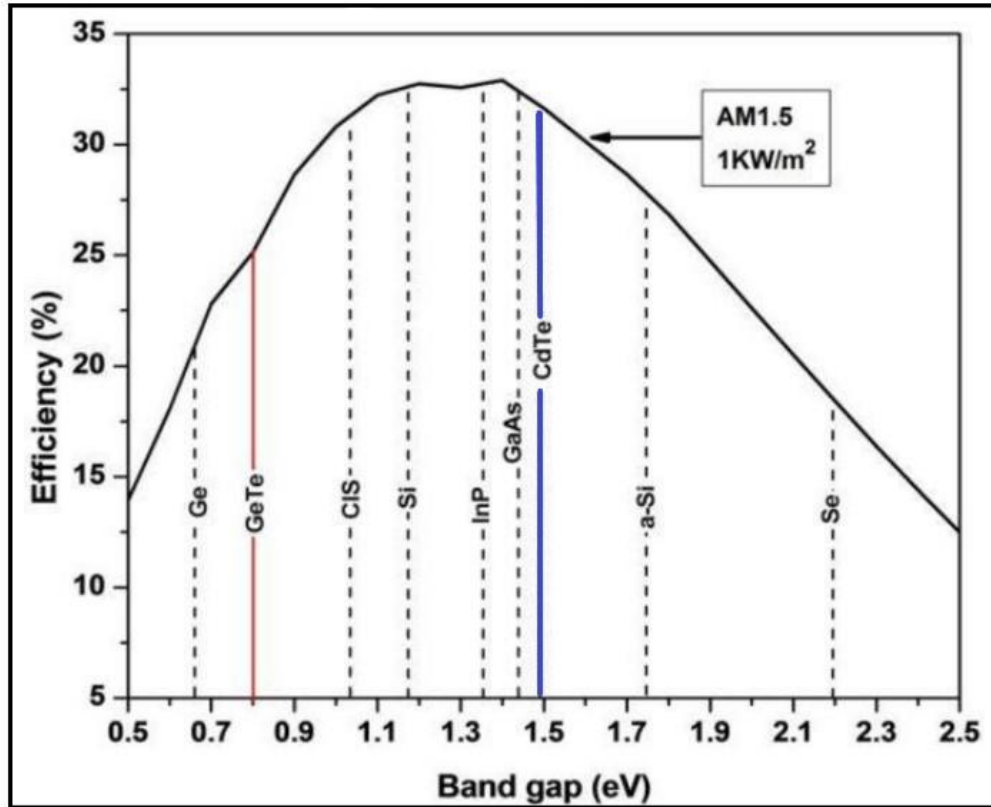
Figure 7: Shockley-Queisser Limit for theoretical efficiency. The CdTe band gap is shown around 1.5 eV (solid blue line). Image modified from [21].

1.4 Motivation and Research Objectives

Increased efficiencies over the past several years can be attributed to better interfaces. The back contact has an important contribution to device performances. Losses can stem from high-resistance layers, unfavorable band alignment (valence band), or a combination of the two [22]. The motivation for this research was to improve device efficiency and to improve device stability.

1.4.1   New Back Contact Development

The goal of this research was to develop a back contact that was similar to solar modules developed in industry. The processes explored utilized sputtered metals and sputtered metal

oxides or nitrides. Not only did this research focus on the back contact, but it also explored aluminum as a back electrode.

1.4.2 Improved Device Stability

The other major goal of this research was improved stability. PV device stability is an important factor in performance. Device performance over time is another important aspect that was considered.
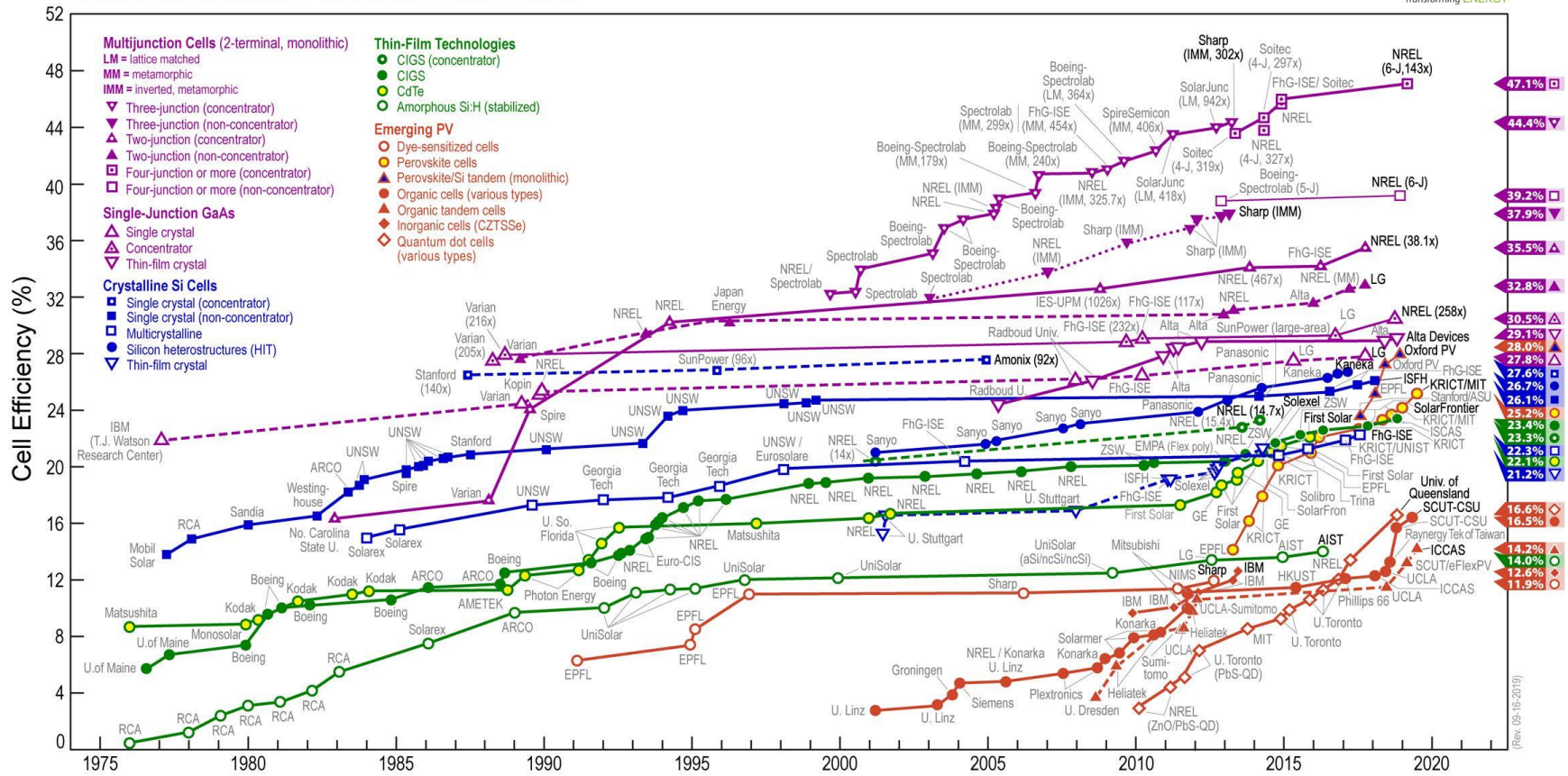
Figure 8: NREL solar cell research efficiencies. Figure referenced from [23].

2   THIN FILM CDTE DEVICE STRUCTURE

2.1 Device structure for a standard baseline device

Utilizing a superstrate configuration, devices were fabricated on NSG Tec 10 soda lime glass. The Tec 10 glass has a fluorine-doped tin oxide layer deposited by the manufacturer. The tin oxide layer is the transparent conducting oxide (TCO).

Glass substrates were cleaned with an ultrasonic cleaner using an industrial grade detergent. Clean glass samples were kept in a desiccated storage area. The Tec 10 samples were stored between several hours to several days until they were used. Utilizing an RF magnetron, a layer of magnesium zinc oxide- $Mg_xZn_{1-x}O$ (MZO) was deposited by sputtering. This layer (typically 100 nanometers thick) has no intentional substrate heating. MZO is a high-resistance transparent (HRT) oxide layer. Previously, cadmium sulfide (CdS) was used in CdTe devices as the buffer layer, however the HRT layer has proven higher efficiencies. The HRT layer allows shorter wavelength light to be better utilized than in CdS by having a higher current generation. With better band alignment to CdTe, the HRT layer (11% MgO weight percent, 89% ZnO) improves fill factor and V_{OC} [24].

After the deposition of the MZO layer, samples were stored in a vacuum desiccator until the CdTe layer. CdTe sublimation occurs in a vacuum chamber with multiple deposition sources [25]. This single vacuum chamber is referred to as the Advanced Research Deposition System (ARDS). The ARDS has multiple sources with multiple materials such as preheat, CdTe, cadmium selenium telluride -$CdSe_xTe_{1-x}$ (CST), cadmium chloride ($CdCl_2$), and a bake out source. The MZO sample was preheated to ~530°C before entering the CST source and then the CdTe source. The CST and CdTe process temperatures were high enough to sublimate the materials onto the glass sample. These process temperatures were held constant to allow for a

more controlled sample thickness. After the CdTe deposition, $CdCl_2$ passivation was performed while still under vacuum. The $CdCl_2$ process was performed with the sample slightly hotter than the source temperature. After a long passivation period and annealing, the sample cooled in vacuum for 180 seconds. The substrate was then removed from vacuum and the film surface was rinsed with deionized water to remove excess $CdCl_2$.

Copper chloride deposition was the next step for each sample. The sample was preheated to allow for uniform deposition of copper chloride (CuCl) across the device. The sample then underwent CuCl treatment and was annealed. Variations of copper processes were performed throughout this research.

The standard device then receives a layer of evaporated tellurium (~20-50 nm). The standard device was then finished with carbon and nickel paint in a polymer binder to form the back electrode. At this point, standard baseline devices are finished and ready for testing. A standard device is shown in Figure 9.

CdCl$_2$ treatment

CuCl treatment

Tec 10 Glass Substrate

SnO$_2$:F TCO

Mg$_x$Zn$_{1-x}$O

100 nm

Graded CdSe$_x$Te$_{1-x}$ / CdTe

4.0 μm

Te

30 nm

C paint in a polymer binder

Ni paint in a polymer binder
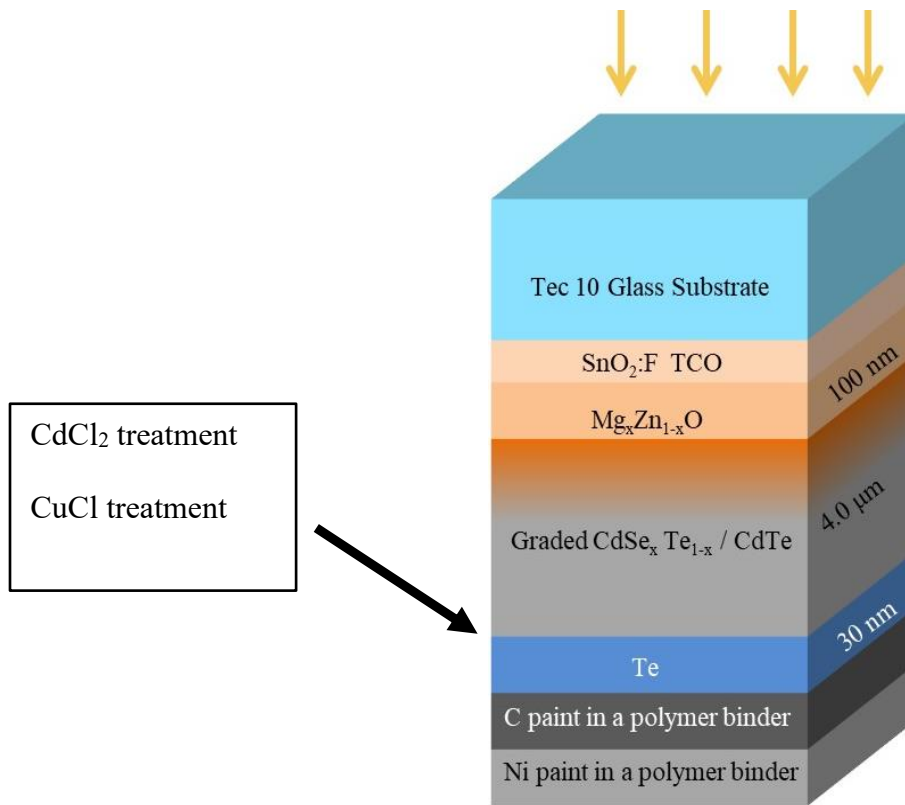
Figure 9: Device structure for standard, baseline devices.

2.1.1   Back Contact

Purpose of Back Contact

Good back contacts in p-CdTe are difficult to find. CdTe has a very high electron affinity which makes it difficult to form a back contact without a Schottky barrier,

Copper Doping

Copper doping is a critical part of CdTe devices. Copper has been used as a back contact for CdTe devices as it aids in increasing carrier concentrations at the back of the device, thus reducing the potential barrier [26]. The copper at the back results in an increased saturation current density.

16

Stable Back Contact Techniques

In order to obtain a stable back contact, materials selection can be critical. Often, materials are selected with similar or higher electron affinity than p-CdTe. The higher electron affinity allows for better band alignment.

After device or film fabrication, several techniques were used for characterization as described in sections 2.2 and 2.3.

2.2 Materials Characterization

Materials characterization was a very important aspect of this research. Each characterization technique helped with understanding material, chemical, and microstructural properties.

2.2.1 Four-point Probe Resistivity

Four-point probe resistivity measurements were performed. Each film was deposited on a glass substrate. The sheet resistance was measured with the four-point probe. Following the sheet resistance measurement, a film thickness was determined using a profilometer. Using the sheet resistance and film thickness, the resistivity of the film was be determined.

a)   b)
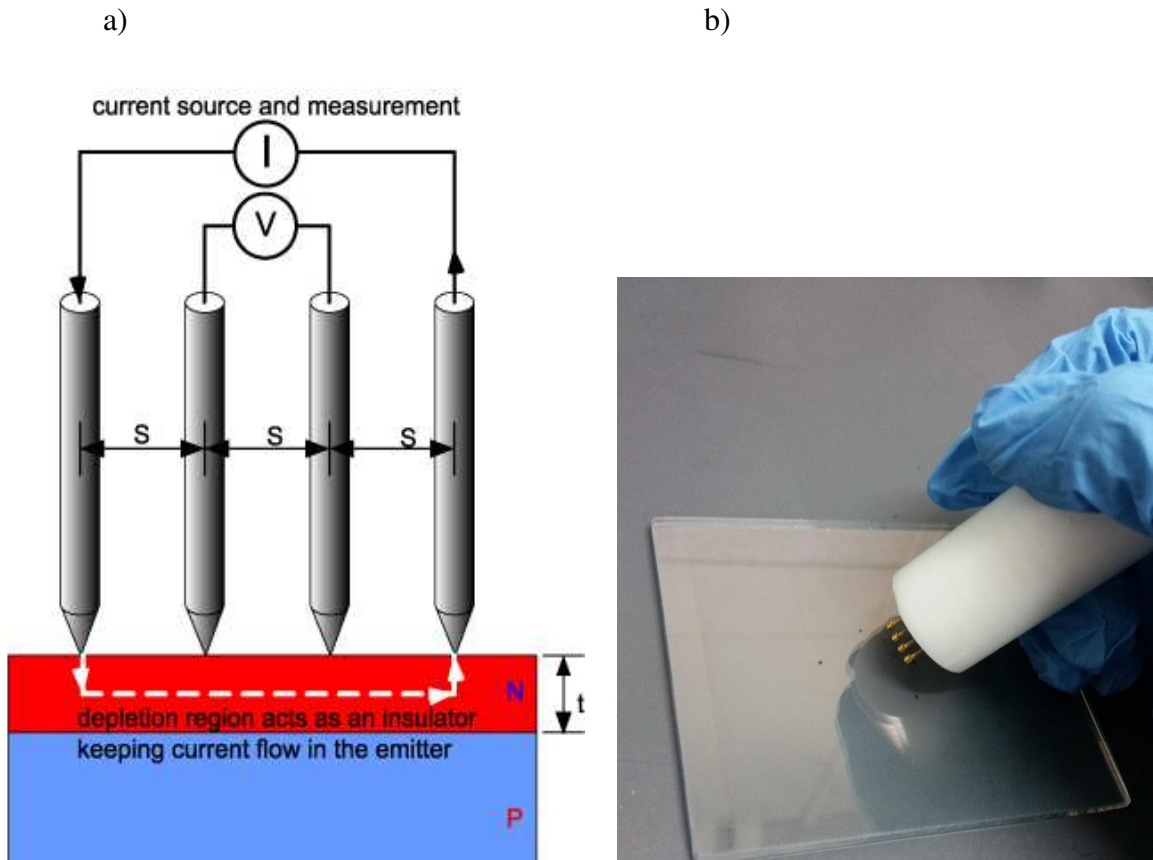
Figure 10: a) Four-point probe measurement system. Figure modified from [27]. B) Four-point probe used to conduct measurements in the lab.

Four- point probe measurements were used to measure the sheet resistance of samples. Measurements of resistance where taken in Ohms per square.

$$\rho_\square \left(\frac{\Omega}{\square}\right) = \frac{\pi}{\ln(2)} * \frac{V}{I} \tag{2}$$

Resistivity measurements for thin films incorporated the film thickness. Since the film thickness is much less than the probe spacing, the following equation was used.

$$\rho(\Omega \ cm) = \frac{\pi}{\ln(2)} * \frac{V}{I} * t \qquad (3)$$

The units of resistivity are Ohm-meter or Ohm-centimeter [27].

2.2.2 Hall Measurements

Hall measurements were performed for several reasons. One reason is to determine the carrier mobility. The carrier mobility varies with respect to temperature, the dopant concentration level, carrier type, and type of semiconductor. Carrier mobility can be how quickly charge carriers move when an electric field is present [28].

2.2.3 X-Ray Photoelectron Spectroscopy (XPS)

X-Ray Photoelectron Spectroscopy (XPS) is a surface sensitive technique that can be very useful for material characterization. XPS can help determine material composition and differences in binding energies. Using x-ray photons to ionize atoms, the ejected photoelectrons can then be measured by their kinetic energy. Each element has a unique energy associated with their core electron binding energies. From the peak binding energies, material properties can be determined from surface state changes. One example of a surface change is oxidation. XPS can be used to measure the sample depth up to ten nanometers [29].

2.2.4 Grazing Incidence X-Ray Diffraction (GIXRD)

X-ray diffraction can be useful in providing material information about crystal structure, chemical composition, and physical properties of materials. One major benefit of XRD is that it is a nondestructive process [30]. GIXRD is a useful technique for thin-films as it allows for strong peak intensities to be measured without interference from the substrate. This is accomplished by having a fixed angle of incidence for incoming x-rays. The detector then scans the range of 2θ, measuring x-rays [29].

2.3 Device Characterization

Several different types of device characterization were performed to determine different parameters of each solar cell.

2.3.1   J-V Light and Dark

Current Density-Voltage (J-V) testing allows for a quick determination of several different parameters. Device characteristics such as open-circuit voltage (V_{OC}), short-circuit current (J_{SC}), fill factor, and efficiency can be determined from a simple J-V test [31]. J-V measurements should be performed at standard conditions of 25°C and 100mW/cm^2 AM 1.5 spectrum [31].

J-V measurements were completed using the solar simulator measurement system Figure 11. This system consists of an ABET Technologies 10500 solar simulator, a Keithley 2402 Source Meter, and an imaging webcam. The J-V measurement system utilizes a LabVIEW VI to monitor measurement parameters, record data, and output text file measurements. The area of each sample was measured with the webcam and recorded in the LabVIEW VI. The sample was then measured under the solar simulator at approximately one sun. Measurements are made by sweeping the voltage from -0.8 to 1.2V in 25mV increments.
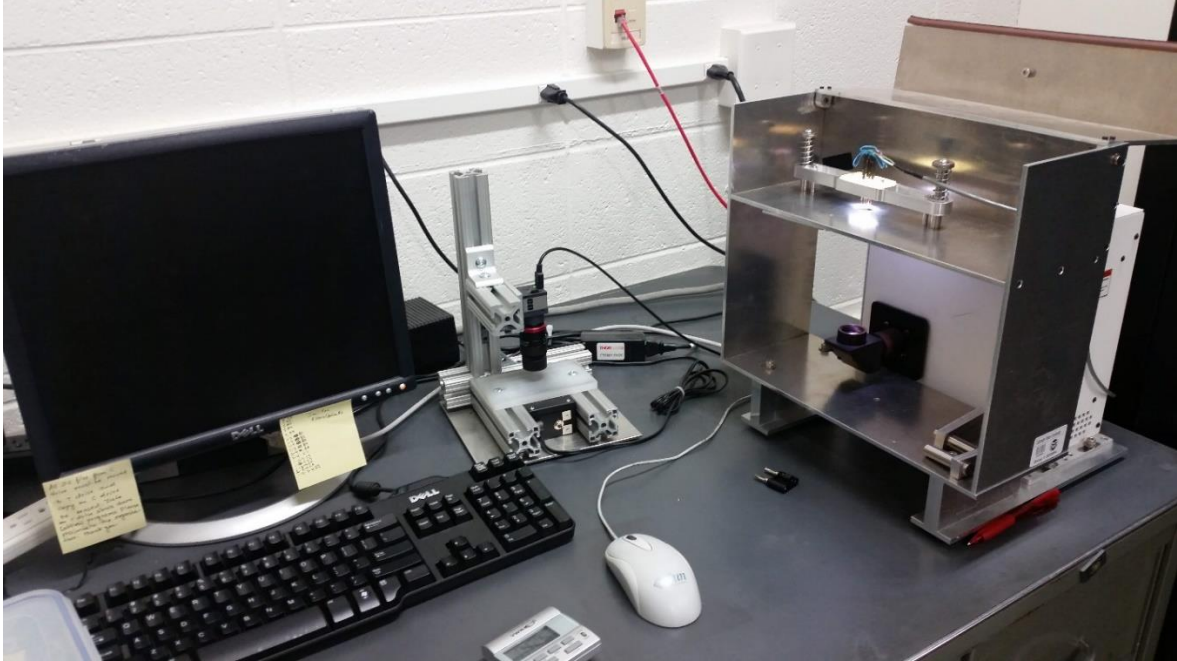
Figure 11: Solar simulator J-V measurement system.

The V_{OC} is measured at the point where the current density is zero. The J_{SC} is measured at the point where the voltage is zero. The J_{SC} and V_{OC} can be used with the voltage at maximum power (Vmp) and current at maximum power (Jmp) to determine the fill factor (FF).

$$FF = \frac{Jmp*Vmp}{J_{SC}*V_{OC}} \qquad (4)$$

The fill factor is a measurement of squareness regarding the J-V curve. The device efficiency is measured using the input power (P_{in}) and the V_{OC}, J_{SC} and fill factor. Efficiency (η) is defined:

$$\eta = \frac{J_{SC}*V_{OC}*FF}{P_{in}} = \frac{Jmp*Vmp}{P_{in}} \qquad (5)$$

Figure 12 displays the common J-V parameters in the form of a diode curve (dark J-V curve), a light J-V curve, and a power density curve.
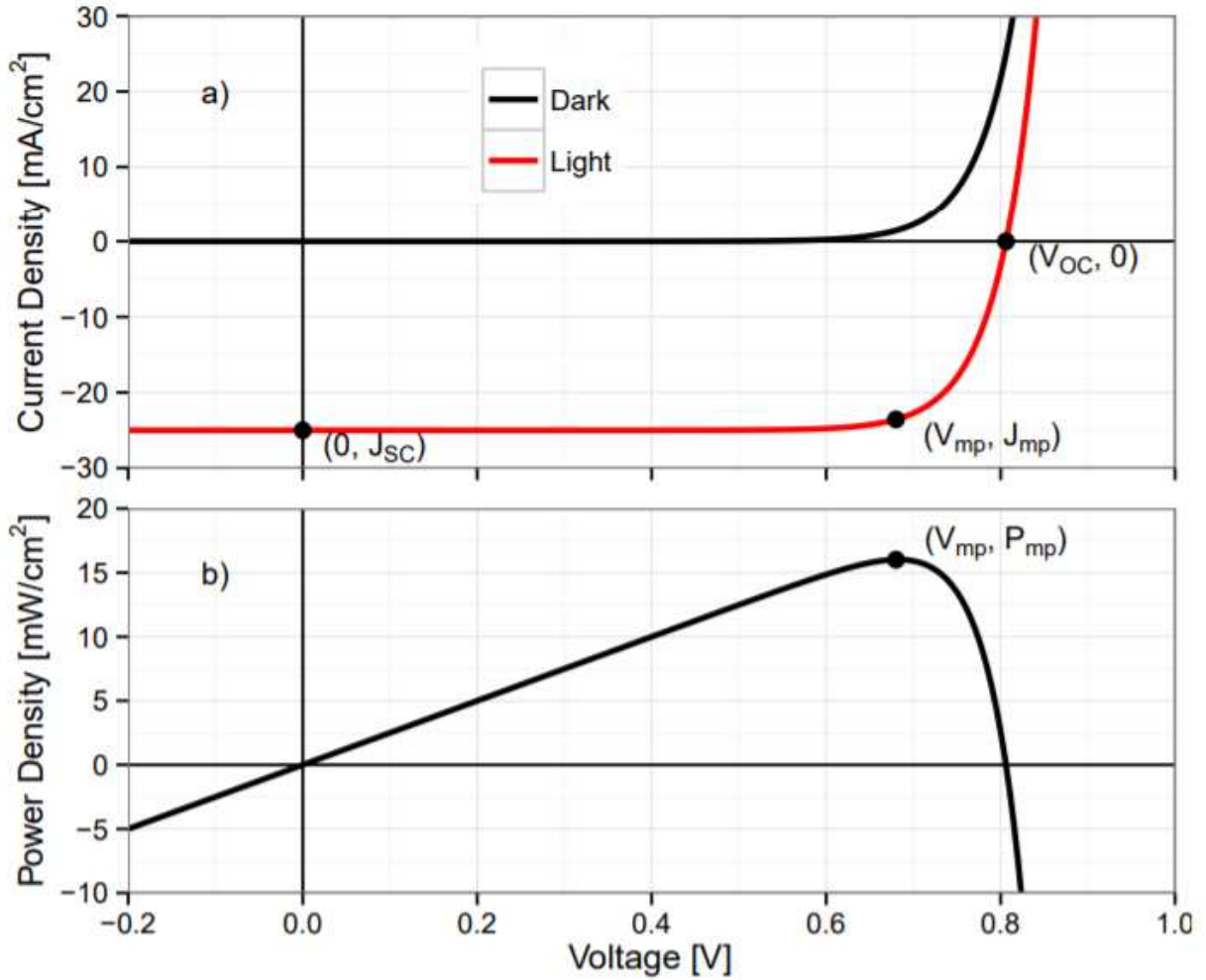
Figure 12: a) Current density vs. voltage plot with light and dark J-V curves. b) Power density vs. voltage curve. Figure referenced from [24].

2.3.2 Quantum Efficiency (QE)

Quantum efficiency can be a useful measurement tool in verifying the short-circuit current and determining different loss mechanisms [29]. The major loss mechanisms in QE are optical and electronic losses. Optical losses include reflections from different layers of the solar cell. Electronic losses are typically caused by recombination in the absorber. While making QE

measurements, electronic losses can be differentiated from optical losses by applying voltage biases to the sample [31].

Measurements can be made using external quantum efficiency (EQE) which is the number of electrons collected per incident photon or by internal quantum efficiency which is the number of electrons collected per the number of absorbed photons. Often the TCO and emitter layers (MZO) absorb photons. In order to allow the most light into the absorber layer, the emitter often has a very high band gap or is a very thin layer often both occur to maximize electron collection. In CdTe, photocarrier collection is limited by minority carrier electrons in the absorber layer [31].

2.3.3 Capacitance measurements

Capacitance –voltage (C-V) profiling is a useful measurement technique for CdTe devices. The C-V measurements are plotted as carrier density as a function of depletion width. In general, on CdTe devices, the output is a distinct U-shaped profile.

Three assumptions were made in order to satisfy the C-V profiling in CdTe solar cells. The first assumption made was that that all space charges were from ionized shallow levels in the depletion region. However, in CdTe, this is not always the case. There may be space charge from the many shallow levels and deep levels in the depletion region. These levels may be impacted by intrinsic defects in the CdTe grains or the extrinsic impurities of possible chlorine or copper [32].

The second assumption made was the existence of only one semiconductor while performing the experiment. This implies that there is a p-n junction or a Schottky device with minimal influence from the back contact. For the p-n junction, there must be ohmic contacts. If there is a Schottky device, the second contact must be ohmic [32].

The third assumption is that the semiconductor is thick enough to complete full measurements. A possible concern is in thin CdTe devices, the entire p-n junction could be the depletion region rather than the assumed situation of a quasi-neutral region (no electric field) next to the depletion region [32].

Capacitance–frequency (C–f) measurements are done before C–V measurements. C–f measurements can be used to determine trap states in the depletion region [33]. In CdTe, when C–f measurements should be uniform and flat across the frequency that it was measured for each voltage measured. Unless stated otherwise, it can be assumed that the C–f measurements were uniform, and it can also be assumed that the C–V measurements were made at 100kHz.

2.3.4   Photoluminescence (PL)

Photoluminescence (PL) is an optical measurement in which photons of a certain energy are absorbed by a material to create electron-hole pairs [34]. Photons are injected into a material, in this case the CdTe sample, and then re-emits the photons. Often the re-emitted photons are at a lower energy than when initially injected and there are less photons re-emitted. PL is a nondestructive technique that can be used on CdTe films and devices.

2.4 Thin-film Deposition

2.4.1   Physical Vapor Deposition

Physical Vapor Deposition (PVD) describes a variety of vacuum deposition processes for thin films. These processes include pulsed arc, magnetron sputtering, ion beam sputtering, and cathodic arc just to name a few. For this research, RF and DC magnetron sputtering were the primary mechanisms used.

2.4.2 Sputtering

Magnetron sputtering has been used in many different markets. The most common areas in which magnetron sputtering has been used are microelectronics, magneto-optics, strain-gauges, and semiconductors.

Magnetron sputtering has been very appealing to the coating industry for many reasons. The major attractions are due to high deposition rate, excellent adhesion properties, ability to deposit high purity films, the ability to coat difficult materials [35], and easy scalability of magnetron sources from research to production level.

Sputtering on an atomic level is to eject atoms from a target material due to bombardment from high energy particles. This occurs with the magnetron (cathode) has a negatively electrical potential when it is turned on. The ground reference is the chamber (anode). The magnetron emits free electrons that bombard the process gas (typically argon). The free electrons hit the valence electrons of the argon causing the argon atom to become a positively charged ion. This positively charged ion is driven to the negatively charged magnetron. When the positively charged ion hits the target, it liberates a target particle. The target particle is "sputtered" onto the substrate which is directly above the cathode. After hitting the target, the positively charged ion recombines with one of the floating free electrons. When this occurs, a photon is emitted. The constant recombination of positively charged particles with free electrons forms the magnetron plasma [36].

2.4.3 DC magnetron Sputtering

Direct-current (DC) magnetron sputtering is used primarily with metallic targets. There are many advantages to DC sputtering including a significant reduction in cost as compared to RF sputtering. While the magnetron setup is very similar in DC and RF sputtering, the primary

cost savings comes from the power supply manufacturing process. DC magnetrons can operate at power levels around 70W/cm^2, however this is the upper limit for the average power across the target [35].

With metallic targets, oxide layers and contaminates can form on the target surface if it has been exposed to atmospheric conditions. These unwanted layers of contaminates need to be pre-sputtered off the target which is also known as conditioning the target. When the target is conditioned, the material and contaminates are sputtered onto the target shutter. Once contaminates are removed, the target shutter is opened and the substrates are sputter deposited [35].

2.4.4　RF Sputtering

Radio frequency (RF) magnetron sputtering techniques are primarily used for insulating targets. Sputtering with an RF system uses an alternating current at high frequency (~ 13.56 MHz). By alternating the current, this avoids charge build up on the surface of the target. In order to make sure all the power is directed to the plasma; an impedance matching network is needed. RF sputtering has the advantage of being able to sputter metallic and dielectric target materials. However with ceramics and insulating materials the power levels are much lower across the surface of the target (~10W/cm^2) [35].

As with DC sputtering in metallic targets, RF sputtering processes also need to condition targets before depositing materials in order to remove any contaminates or oxide layers on the surface of the target [35].

3   STUDY OF MOLYBDENUM OXIDE AND MOLYBDENUM NITRIDE LAYERS

3.1 Introduction

Molybdenum oxide (MoO_x) and molybdenum nitride (MoN_x) transition metals were explored for several reasons. When looking at the properties of MoO_x and MoN_x, both materials have high work functions, low resistivities, and can be easily sputter deposited. MoO_x and MoN_x are also recolonized for being stable, robust films.

The work function for each material varies. Molybdenum is a transition metal. When focusing on the metal, the work function of molybdenum ranges from 4.36-4.95 eV, which is much different from that of molybdenum oxide or molybdenum nitride [37]. Molybdenum oxide has been found to have a high work function as high as 6.80 eV with some variability [38]–[40]. Molybdenum nitride has a work function of 5.10-5.23 eV [41].

Looking into viability, the MoO_x and MoN_x films could be sputter deposited with a molybdenum target. The oxygen and nitrogen gas contents could be varied from film to film, yet easily controlled.

The resistivity of bulk molybdenum at room temperature is around 5.8 $\mu\Omega$ cm [42]. Resistivity values for thin films vary from bulk values. For room temperature molybdenum depositions, resistivities varied from 10000-20000 $\mu\Omega$ cm [43]. The resistivity of molybdenum nitrides varies greatly due to deposition rate, nitrogen content, crystal orientation and structure, temperature, and several other factors [44].

Molybdenum nitride is a transition metal nitride. When the nitrogen atoms are incorporated into the film, they occupy the interstitial sites as the metallic structure is close-packed [44].

The MoN$_x$ and MoO$_x$ films were used as back contact layers. An example of the device structure can be seen in Figure 13.
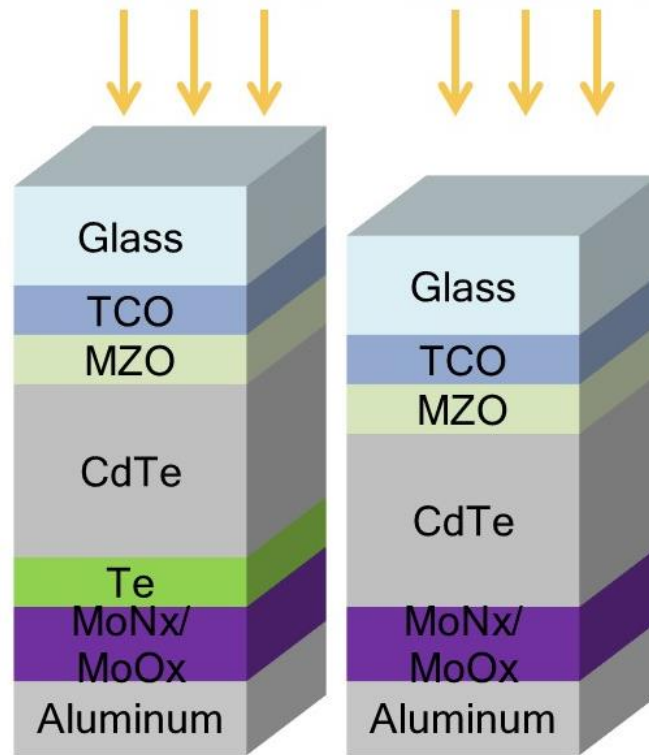
Figure 13: MoN$_x$ and MoO$_x$ structures used for device characterization.

3.2 Experimental Details

3.2.1 Metallization Vacuum Chamber

The metallization chamber was rebuilt by Dr. Jason Kephart and Seth Thompson to be a functioning sputter deposition system for metal back contact depositions. The vacuum chamber utilizes a mechanical pump and a diffusion pump which allows the chamber to reach $5 \cdot 10^{-5}$ Torr pressures. The chamber can reach even lower pressures by flowing liquid nitrogen through the cold trap. With the liquid nitrogen flowing through the cold trap, the chamber has reached $8 \cdot 10^{-7}$ Torr. Figure 14 displays the metallization vacuum chamber apparatus.

3.2.2   Metallization Vacuum Chamber System Updates

While the metallization vacuum chamber was functional, some modifications needed to be implemented. For ease of processes, the chamber was modified to allow two gases to flow into the chamber at one time and to allow for easier single sample depositions.

The implementation of an additional mass flow controller allowed for multiple gases to be used in the vacuum chamber at one time. The primary gas used was argon and the secondary gas varied between oxygen and nitrogen.

Figure 14. Metallization vacuum chamber apparatus.

A sample holder was designed to sit above the 5-cm diameter planar cathode. The sample holder was designed to deposit one sample at a time instead of the traditional rotating 8-sample holder. The single sample holder allowed for quicker depositions and with similar film uniformity across the sample surface. The sample holder was placed 15.2 cm above the deposition target to allow for both film uniformity across the substrate and a high deposition rate as shown in Figure 15.
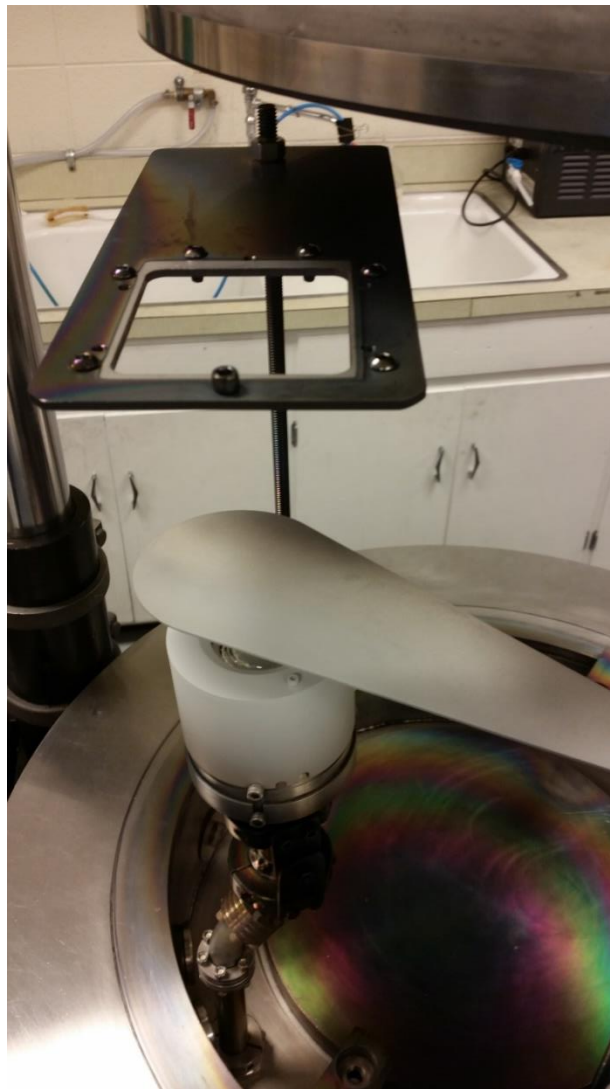
Figure 15: Sample holder and magnetron prepared for deposition.

3.2.3   Deposition Process

The metallization chamber utilizes a DC magnetron to sputter deposit metallic and compound films. Utilizing a metallic target, in this case a molybdenum target, metallic thin films were sputter deposited. Through the addition of another mass flow controller, reactive gases could be added to the process while sputter depositing. The reactive gases used were oxygen and nitrogen to form molybdenum oxide and molybdenum nitride.

Reactive sputtering is the process of sputtering a metallic (elemental) target with chemically reactive gases to form compound and alloy thin films. The reactive gases interact with the target surface and the emitted target material [45], [46].

Different film compositions were deposited. Films were deposited at pressure of 10 mTorr and with no intentional substrate heating. Maintaining constant pressure, the gas flow rate varied slightly for each deposition. By ratioing the oxygen to argon and the nitrogen to argon during the deposition, there were 10%, 20%, and 40% O_2/Ar and N_2/Ar films. In addition to the oxygen and nitrogen containing films, a molybdenum film was deposited with no intentional reactive gases. After the films were deposited, they were immediately placed in a glovebox filled with argon to minimize surface contamination.

3.3 Results

3.3.1   Materials Characterization

Initial depositions began with material characterization. The general post deposition characterization always included measuring deposition rate and resistivity. After refining the deposition process, Hall measurements, XPS, and GIXRD were performed.

General Post Deposition Characterization

3.3.1.1 Deposition Rate and Four-point probe

For each film, the deposition rate was calculated. The deposition rate for the Mo film was

very low as compared to the other films. Once oxygen was incorporated at a 10% O_2/Ar, the

deposition rate increased. The deposition rated decreased with increasing oxygen concentration.

With the nitrogen containing films, the deposition rate was constant.

From the measured thickness, the average resistivity across the plate was calculated with

the four-point probe. The average resistivity for Mo was low for this experiment, but was

relatively high as compared to the bulk molybdenum resistivity of $5.8*10^{-6}$ Ω cm [42].

Resistivity increased with increasing oxygen content and with increasing nitrogen content in

each film. A summary of deposition rate and resistivity for each film can be found in Table 1.

Each film thickness was several hundred nanometers thick which allowed for sufficient thickness

when measuring resistance.

Table 1: Summary of deposition rate and resistivities for the molybdenum containing films.

% O_2 or % N_2 during sputter deposition	Deposition Rate nm/s	Average Resistivity Ω-cm
Mo	0.26	$2.7*10^{-4}$
10% O_2/Ar	0.55	$4.8 *10^{-2}$
20% O_2/Ar	0.46	2.1
40% O_2/Ar	0.35	14.9
10% N_2/Ar	0.30	$1.4 *10^{-3}$
20% N_2/Ar	0.25	$1.7*10^{-2}$
40% N_2/Ar	0.30	$5.7*10^{-2}$

3.3.1.2 Water solubility test

Additional research has been done on the effect of defects in MoO_x on hole transport [38]. After molybdenum oxide is deposited, the chemical state of an oxide layer could be MoO_2, MoO_3 or a combination of chemical compounds. MoO_2 is a metallic conductor while MoO_3 is typically resistive, transparent, and water sensitive. To obtain MoO_2 or MoO_3, the film conditions depend on partial oxygen pressures, and substrate temperatures. When changing from MoO_3 to MoO_2 in the band gap, defect states tend to emerge with increasing oxygen vacancies [47].

If MoO_x films are exposed to air, humidity, or change in temperature, added stresses can be observed in the film and the film can have a significant decrease in work function [40], [48].

Samples were tested to determine which composition of MoO_x was deposited. With increasing oxygen content, the MoO_x films become more transparent from left to right as seen in Figure 16 a. and b. The film made without oxygen is a metallic gray, the 10% and 20% O_2/Ar samples are brown and slightly transparent, and the 40% O_2/Ar sample was almost completely transparent with a slight blue color.

To test if the highest-oxygen film was predominately MoO_3 (water-soluble), the films were placed in a beaker of deionized (DI) water. The 40% O_2/Ar film changed after several minutes in the water. The blue film transformed to more of a light brown, yet still transparent film. After 2 hours, the films were removed from the deionized water. The 40%O_2/Ar sample was completely transparent. The samples made with 10% and 20% O_2/Ar had dissolved partially and the films had a lighter color than originally deposited. The molybdenum film with no intentional oxygen had no visible change. All samples can be seen after treatment in Figure 16 c. and d.
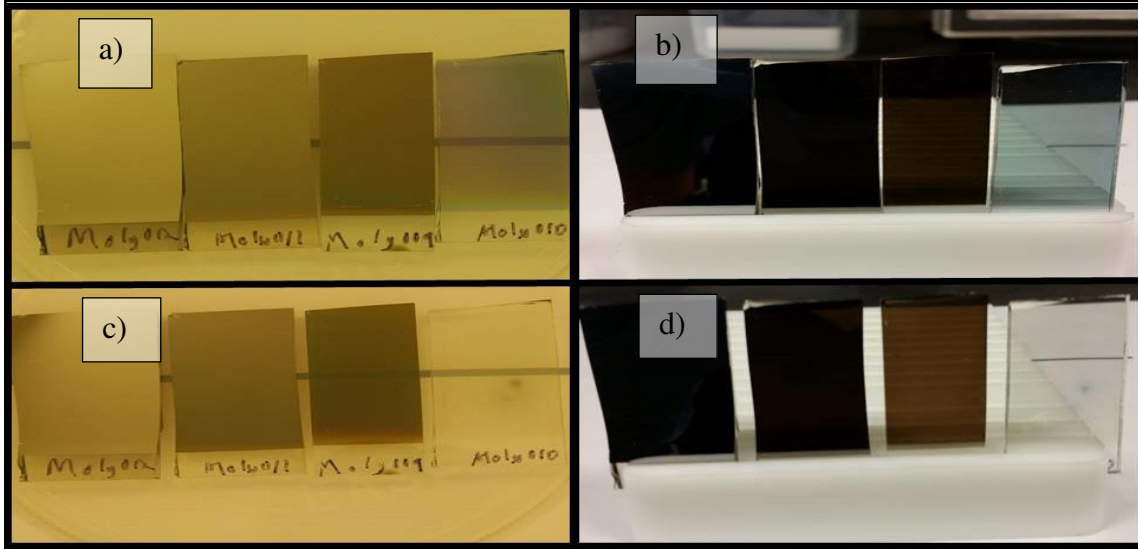
Figure 16: a) Left to right: As deposited -molybdenum, 10%, 20%, and 40% O_2/Ar contents. b) Top: As deposited films at a different angle. c) Left to right: samples after a two-hour DI water treatment- molybdenum, 10%, 20%, and 40% O_2/Ar contents. d) Samples after DI water treatment- films at a different angle.

From the water solubility experiment, it was determined that the MoO_x films were a mixture of MoO_3. As the oxygen concentration in the film increased, the amount of MoO_3 in each film increased. The 40% O_2/Ar film was primarily determined to be MoO_3 with some intermixing of chemical compounds.

3.3.1.3 Hall Measurements

Hall measurements were performed to determine bulk concentration and mobility of carriers. The accuracy of the resistivity measurements from the four-point probe were also confirmed. The resistivity measurements vary slightly from the four-point probe; however, the measured values were still reasonable. In an ideal situation, the bulk for each sample, the bulk concentration would be high, and the carrier mobility would also be high for each sample.

Table 2: Hall measurements for 100nm Mo, MoO$_x$, and MoN$_x$ films.

Sample	Current	Bulk Concentration (1/cm^3)	Mobility (cm^2/Vs)	Measured Resistivity ($\Omega - cm$)
Mo	3 mA	7.49E+22	1.11E-01	7.48E-04
10% O$_2$/Ar	1 mA	1.60E+22	7.74E-03	5.03E-02
20% O$_2$/Ar	100 μA	8.76E+20	2.46E-02	2.90E-01
40% O$_2$/Ar	10 nA	1.08E +14	5.69E+01	1.02E+03
10% N$_2$/Ar	3 mA	2.44E+22	1.50E-01	1.71E-03
20% N$_2$/Ar	1 mA	3.40E+21	5.93E-02	3.09E-02
40% N$_2$/Ar	1 mA	6.33E+22	3.75E-03	2.63E-02

3.3.1.4 XPS

XPS measurements were performed on the Mo, MoO$_x$, and MoN$_x$ films. Table 3 has experimental binding energy values from literature for similar chemical compounds and valence shells.

Table 3: XPS values from literature.

	Valence Shell	K	M	M	M	M	
	Valence Sub-Shell	1s	3p$_{1/2}$	3p$_{3/2}$	3d$_{3/2}$	3d$_{5/2}$	Reference
Element	Formula	Binding Energy (eV)					
N	N	409.9					[49]
Mo	Mo		411.6	394.0	231.1	227.9	[49]
Mo	MoO$_2$				232.6	229.5	[50]
Mo	MoO$_3$				235.6	232.5	[51]
Mo	MoN					228.1	[52]

While the measured XPS data was fitted, each energy orbital was found to be several combinations of energy peaks. The molybdenum 3d peak in XPS was used to determine peak curves in different bonding environments due to oxygen or nitrogen incorporation.
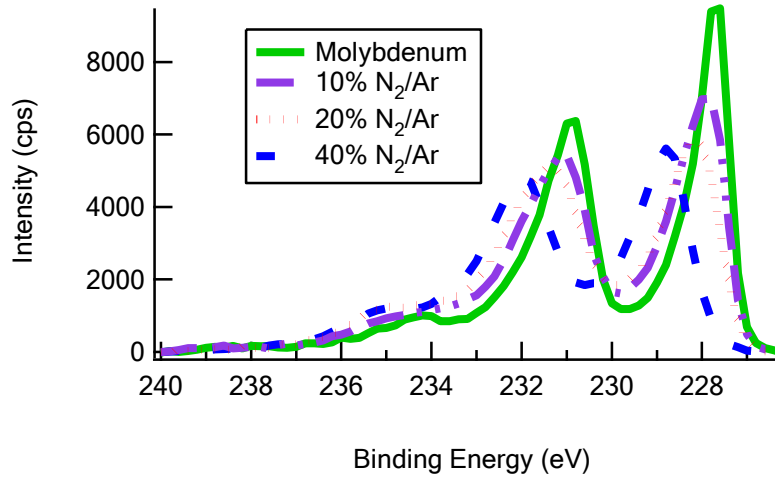
Figure 17: XPS spectra for the molybdenum 3d peak showing nitrogen incorporation into the film.
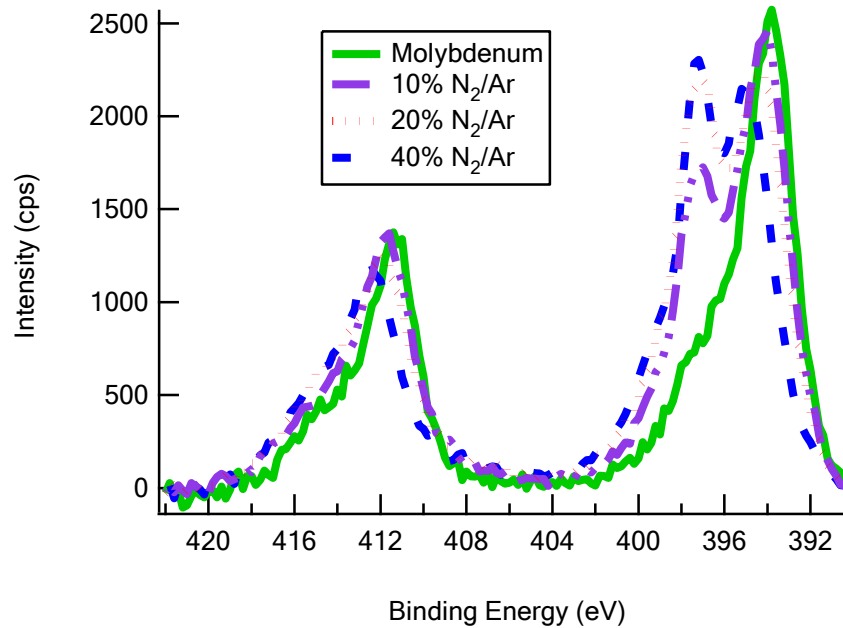
Figure 18: XPS spectra for molybdenum 3p peak showing nitrogen incorporation.

The XPS spectra for the molybdenum oxide films displayed a strong shift in binding energy with increasing oxygen content. For the 10% O_2/Ar and 20% O_2/Ar films there are several combinations of peaks along the spectrum as seen in Figure 19.
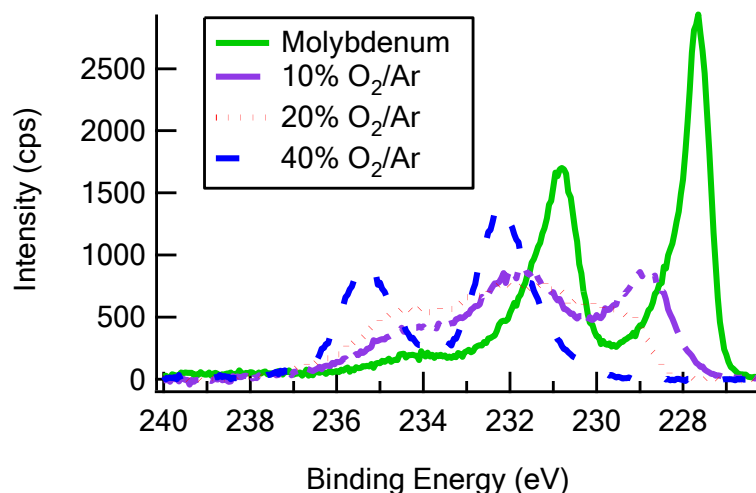
Figure 19: XPS spectra for molybdenum 3d peak showing oxygen incorporation.

3.3.1.5 GIXRD

From the GIXRD measurements, it was determined that the MoO_x films with any additional oxygen were determined to have amorphous-like supporting the complex mixture of XPS binding energies. The MoN_x films had some crystalline structure. The MoN_x films were compared with the JCPDS cards for Mo and Mo_2N structures.
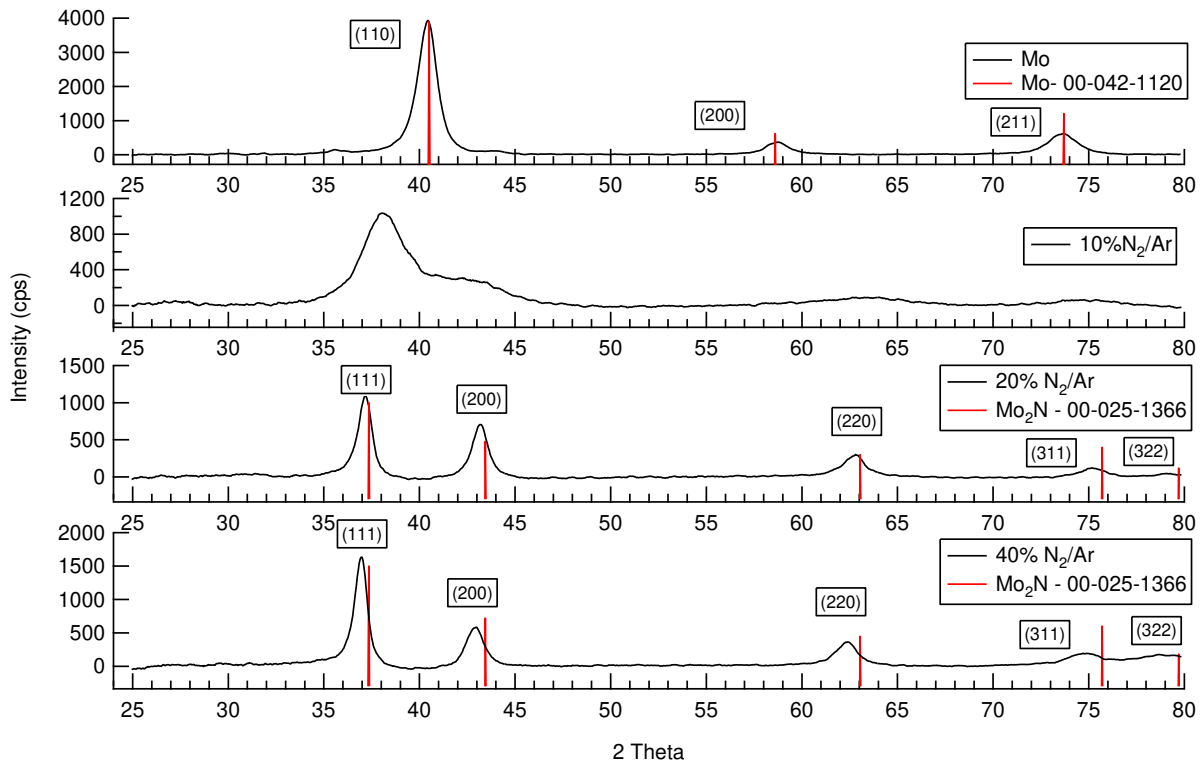
Figure 20: GIXRD spectrum for molybdenum nitride films.

3.3.2 Device Characterization

3.3.2.1 J-V Light Testing

When looking at the device performance, there are a few trends in the results. Device structure is the same initially with MZO, CdTe, CdCl$_2$ and CuCl. After the copper treatment, device structure varies. The first back contact is a baseline device with nickel paint. Each sample had a half plate of tellurium and a half plate without tellurium. With tellurium, the baseline device has a high V$_{OC}$ and fill factor. Without tellurium, the baseline device has a high V$_{OC}$, but the fill factor is very low indicating a need for a buffer layer. One of the major limiting factors of a solar cell is the V$_{OC}$. The V$_{OC}$ can be limited by recombination currents in the space-charge

region or by interfaces. The interfaces between the MZO/CdTe and CdTe/back contact are critical [31].

The device with only a sputtered aluminum back contact/electrode had poor performance in V_{OC} and fill factor with and without tellurium. With the addition of a molybdenum, MoO_x, or MoN_x layer, the device performance significantly increased as compared to the aluminum only case. The molybdenum, MoO_x, or MoN_x layers with tellurium were difficult to distinguish a significant difference in V_{OC} and fill factor. Without the tellurium layer, a molybdenum/aluminum and 10% O_2/Ar MoO_x/ Al device appeared to be similar. With increasing oxygen, the V_{OC} had a steady downward trend in performance. The fill factor also started to follow the same trend, however the loss in fill factor was more gradual. Devices with MoN_x increased device performance with increasing nitrogen concentration. The V_{OC} with and without tellurium was nearly identical and the fill factor overlays as well as seen below in Figure 21.
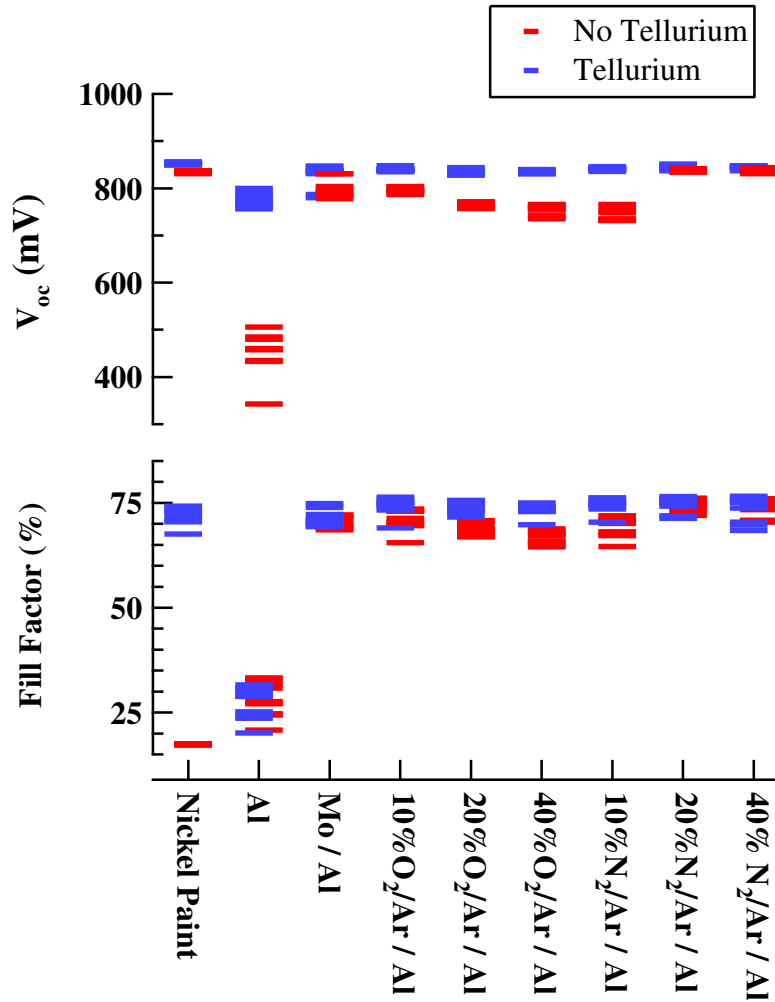
Figure 21: Device performance with 100nm layer of molybdenum, MoO_x, or MoN_x followed aluminum deposition.

The top two devices from the figure above have $20\%N_2/Ar$ and $40\%N_2/Ar$. Devices without tellurium are compared to the baseline with Te/Nickel paint. The devices practically overlay and are only marginally different in J_{SC}. Figure 22 displays the J-V curve for the best devices in the run.
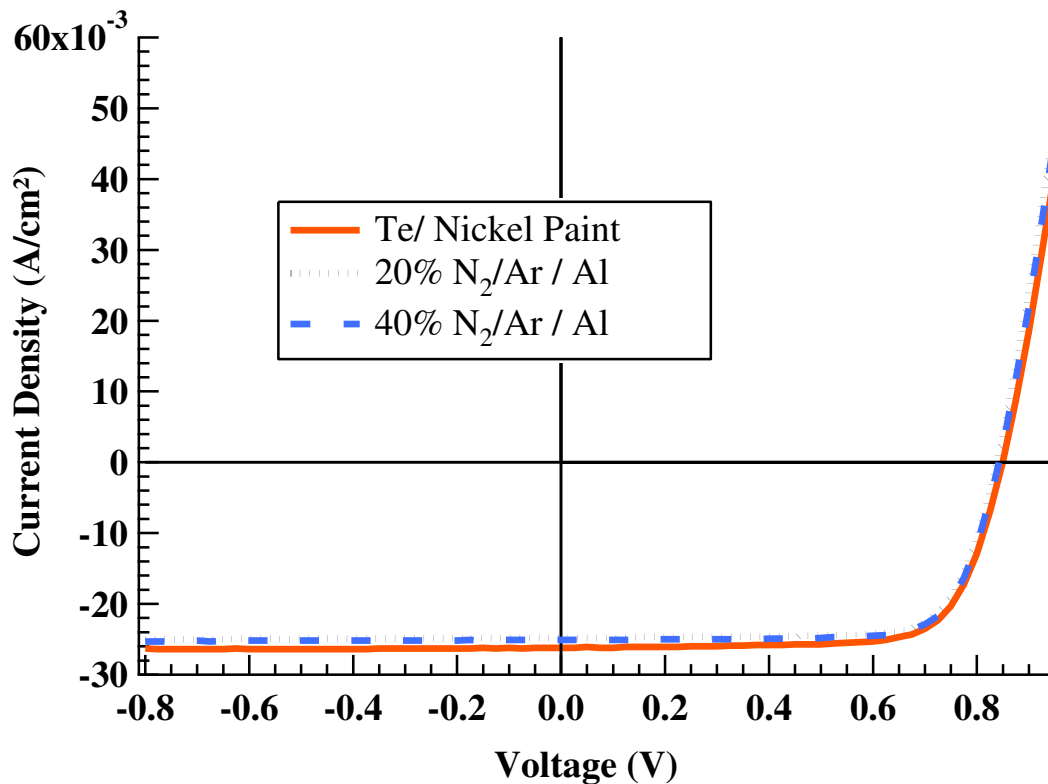
Figure 22: Device performance for the best two devices without Te compared with the baseline device.

Taking the most promising device (40% N_2/Ar /Al) and sweeping the thickness, there was a clear trend that with increased MoN_x thickness, there was increased V_{OC} and increased fill factor. The thickness was swept from 5nm to 200nm. The best performance was from the 200nm MoN_x device. With and without tellurium, the V_{OC} and fill factor were very comparable to the baseline device with Te/ Nickel paint.
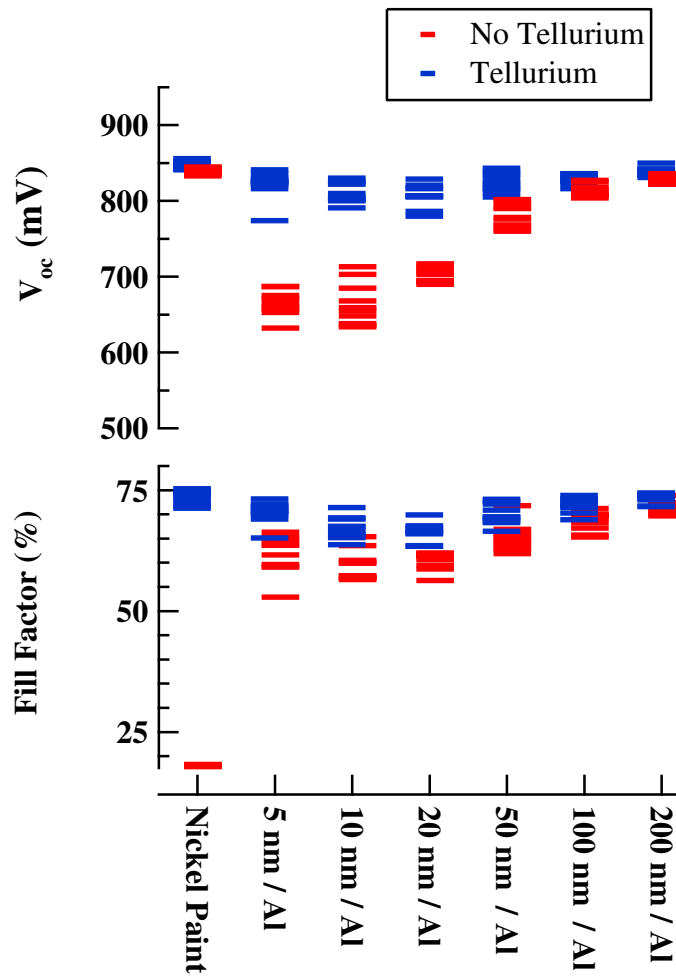
Figure 23: Device performance as thickness increases for the 40%N_2/Ar MoN$_x$ film.

The J-V curves display trends of overlapping similiarity. The comparison baseline device with Te and nickel paint had a slightly higher fill factor than the MoN$_x$/Al devices. However, the V_{OC} and J_{SC} were nearly overlapping as seen in Table 4.
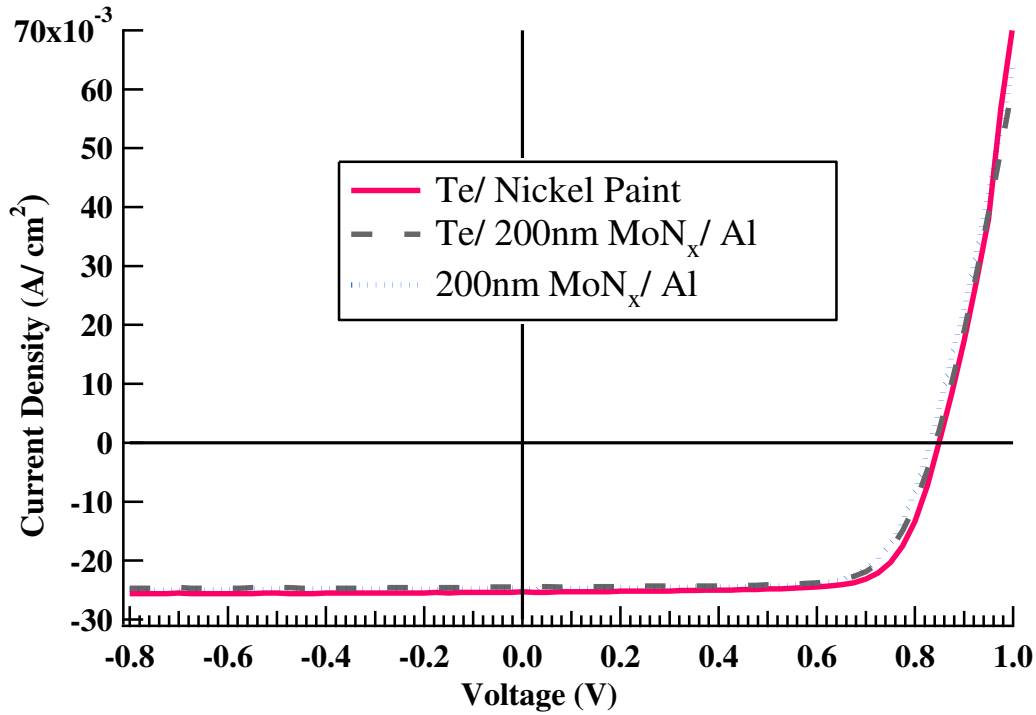
Figure 24: Device performance for the best 40% N_2/Ar MoN_x samples with and without tellurium and the baseline with nickel paint.

Table 4: Best performing device results from Figure 24.

Device	Fill Factor (%)	J_{sc} (mA/cm^2)	V_{oc} (mV)	Efficiency (%)
Te/ Nickel Paint	73.2	25.2	836	15.44
Te/ 200nm MoN_x/Al	74.4	24.5	842	15.35
200nm MoN_x/Al	73.9	24.8	831	15.21

It can be clearly seen from the results of the MoO_x and MoN_x study that each material has unique characteristics. It is important to understand the material changes through XPS, GIXRD, Hall measurements, four-point resistivity, and deposition rate measurements. In terms of device testing, the MoO_x and MoN_x films worked as back contacts, however the 40% N_2/Ar MoN_x film was the most effective back contact with the aluminum back electrode.

43

4 STUDY OF ZINC TELLURIDE THIN-FILM LAYERS

4.1 Introduction

Copper diffusion has been found to improve CdTe device performance. However, too much copper has been linked to device degradation and instability [53]. With the addition of ZnTe- based back contacts doped with copper, device reliability significantly increases [22]. ZnTe has a near-perfect valence band alignment with CdTe valence band. ZnTe has a high chemical stability [26]. ZnTe improves the valence band offset allowing a more ohmic and stable back contact [54], [55]. First Solar observed an increase in V_{OC} and FF when adding a ZnTe back contact to their modules [22].

CdTe reliability and stability historically has been linked to back contact stability and copper migration [56], [57]. The ZnTe back contact retards copper diffusion into the device while maintaining a copper rich back surface [58]. The ZnTe back contact improves module efficiency, while creating a robust contact that prevents against thermal degradation and bias driven power degradation [22].

4.2 Experimental Details

Early ZnTe sputtering was attempted using the metallization chamber that the molybdenum experiments were conducted in. A 5 cm ZnTe target was ordered with a copper backing plate. The major concern for running the ZnTe process in this chamber was the use of a DC power supply as ZnTe is resistive material. Due to limited sputter system availability, an attempt was made to deposit films in this chamber.

Several very thin films were successfully deposited on Tec SB glass. While attempting to start the magnetron for an additional experiment, there were several small arcs that occurred. The plasma did not ignite. One final attempt was made to start the magnetron which resulted in a

sustained arc on the target surface (Figure 25). The magnetron was shut down and the chamber was vented.

Figure 25: ZnTe sputtering target after charge buildup on the surface.

The use of a DC power supply was ineffective. ZnTe is very resistive and the ZnTe target build up a charge on the surface, causing target failure. The ZnTe target surface was not able to discharge as with RF magnetron sputtering.

4.2.1 Deposition Process

The bell jar sputter deposition chamber, shown in Figure 26, has many capabilities. The system has substrate heating capabilities up to 400°C. The system has a Varian HS-2 diffusion pump backed by a small mechanical pump. The system can reach measured pressures 1.0 E-05 Torr. The bell jar sputter system was used to deposit ZnTe films. One sample was loaded into the chamber (film side down) with a target to substrate distance of 5-8 cm. The sample heaters and deposition shielding were added around the sample holder. Once the sample was loaded, the chamber was roughed down to 7.0 E-02 Torr. After roughing the chamber, the foreline was turned on and manually the diffusion pump gate valve was opened. The system was pumped

down for at least 40 minutes before turning on the heaters and the deposition gas (Argon).

Sample heating while depositing ZnTe was found to greatly impact material and optical

properties such as carrier concentration, resistivity, and bandgap [59]. With such a large variation

in ZnTe film properties due to temperature effects, device performance also has been found to be

impacted by temperature [26]. ZnTe deposition temperatures were swept from 150- 350°C.

Once the sample reached the deposition temperature, the temperature stabilized for 15 minutes.

Argon gas was the working gas in the chamber at 15mTorr. The vacuum chamber utilized an RF

magnetron for sputtering with a power density of 7.4 kW/m^2. The target was pre-sputtered for 3-

5 minutes before depositing the ZnTe film. After pre-sputtering, the shutter was opened for

several minutes depending on deposition time. Each deposition was calibrated at the beginning

of each run to 100 nm. Typical deposition rates were around 1 nm/s to 1.2 nm/s. After each

deposition, the power supply was turned off and the samples were annealed for 15-20 minutes at

the deposition temperature. The heaters were then turned off, the gas flow was turned off, and

the diffusion pump gate valve was closed. The chamber was then back filled with argon to 40

Torr while the sample cooled. This process of convective cooling took approximately 2 hours for

the sample to reach 60°C. At that point, the sample was cool enough to remove from the vacuum

chamber. After depositing each ZnTe film, materials characterization or device characterization

were performed.
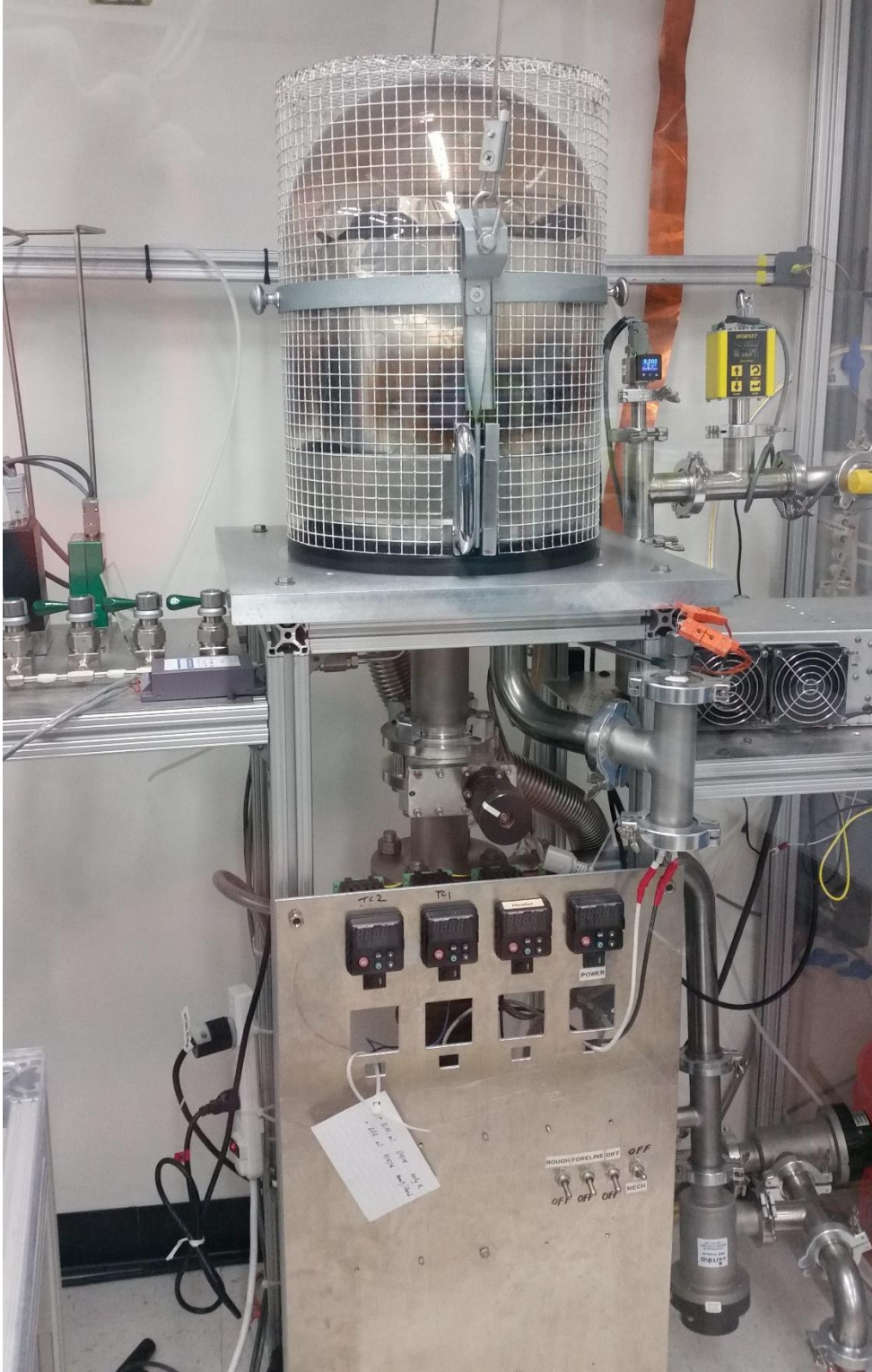
Figure 26: Bell jar vacuum chamber apparatus used for sputter depositing ZnTe thin films.

4.3 Results

The device structure for devices with a ZnTe buffer layer are shown in Figure 27. Device structure is very similar to the baseline, standard device, however the Te layer was replaced with a ZnTe layer.
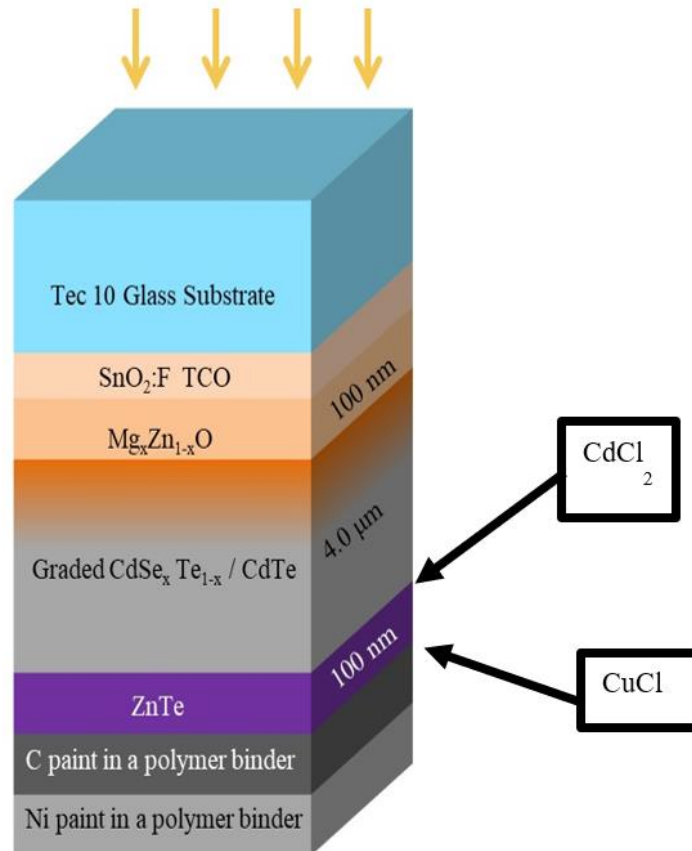
Figure 27: CdTe device structure with ZnTe as a buffer layer.

4.3.1 Material Characterization

4.3.1.1 Four-point probe

Measurements with the four-point probe were attempted on the ZnTe films that were deposited on Tec SB glass (nonconductive glass). The film, regardless of thickness, was always too resistive to record or measure any resistivities. Copper doping was attempted on the ZnTe

films similar to device processing in an attempt to make the film more conductive. The ZnTe: Cu films were too resistive to measure.

4.3.2   Device Characterization

4.3.2.1 ZnTe Temperature Dependence

J-V Light Testing

When ZnTe was deposited at different process temperatures, there was an apparent temperature dependence. It should be noted that after the ZnTe was deposited, the samples were annealed for 20 minutes at the designated deposition temperature. The temperature first improved device performance from 150°C to 250°C. At 350°C the device performance significantly dropped off in terms of current and fill factor. From this study, 250°C was deemed a better process temperature for ZnTe samples. Samples underwent the same standard copper doing process after the ZnTe deposition.
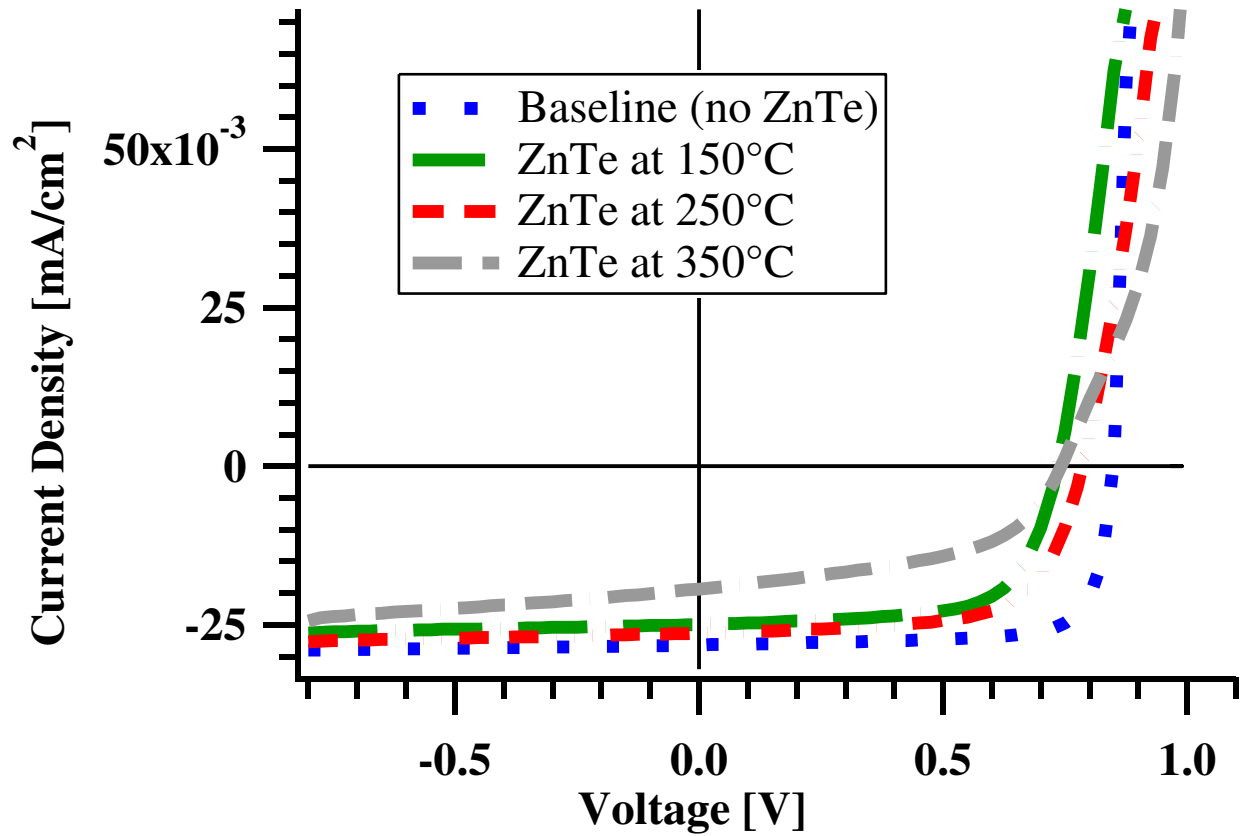
Figure 28: ZnTe deposited at various process temperatures.

EQE

From the EQE results, there is a significant drop across all wavelengths for the ZnTe

sample deposited at 350°C which was reflected by the drop in current in the J-V. For the

baseline, 150°C ZnTe, and 250°C ZnTe devices, performance appeared very similar.
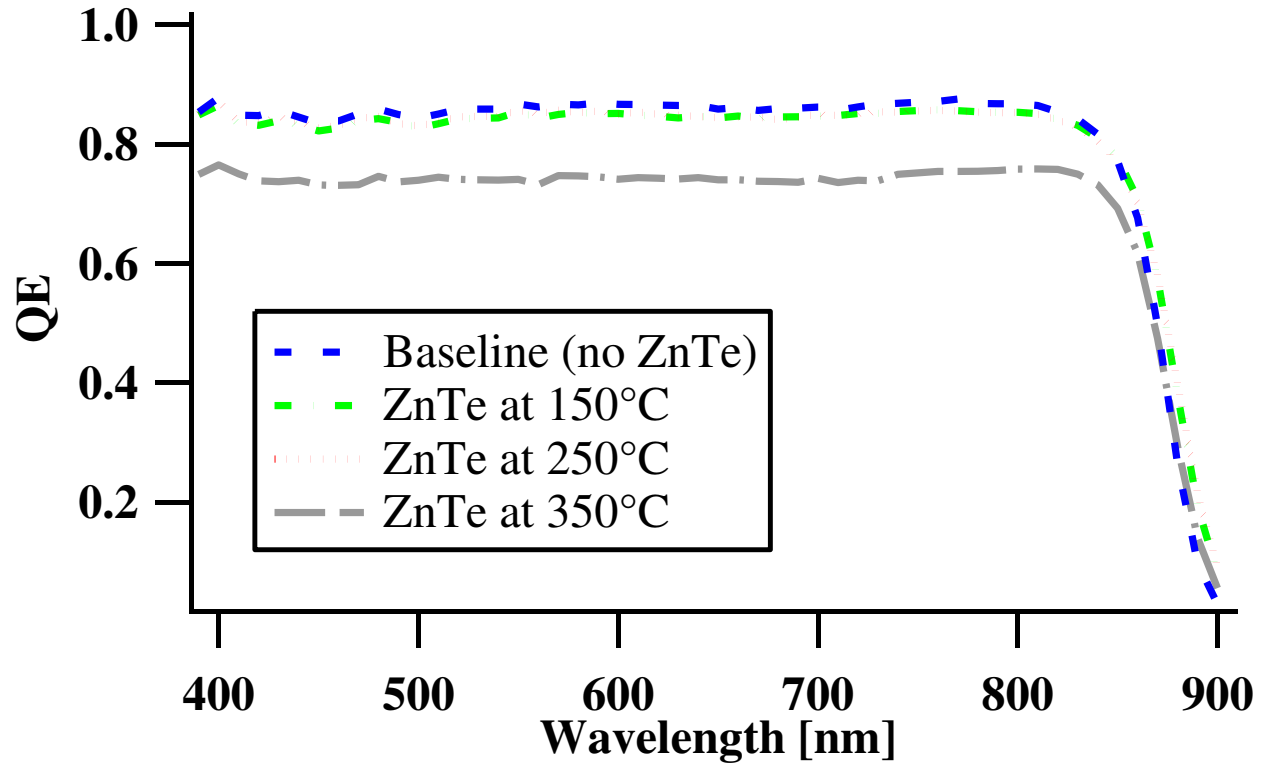
Figure 29: QE results for the various deposition temperatures of ZnTe

C-V Testing

Taking the best device from this study (ZnTe deposited at 250°C) and the baseline

device, capacitance voltage measurements were performed.
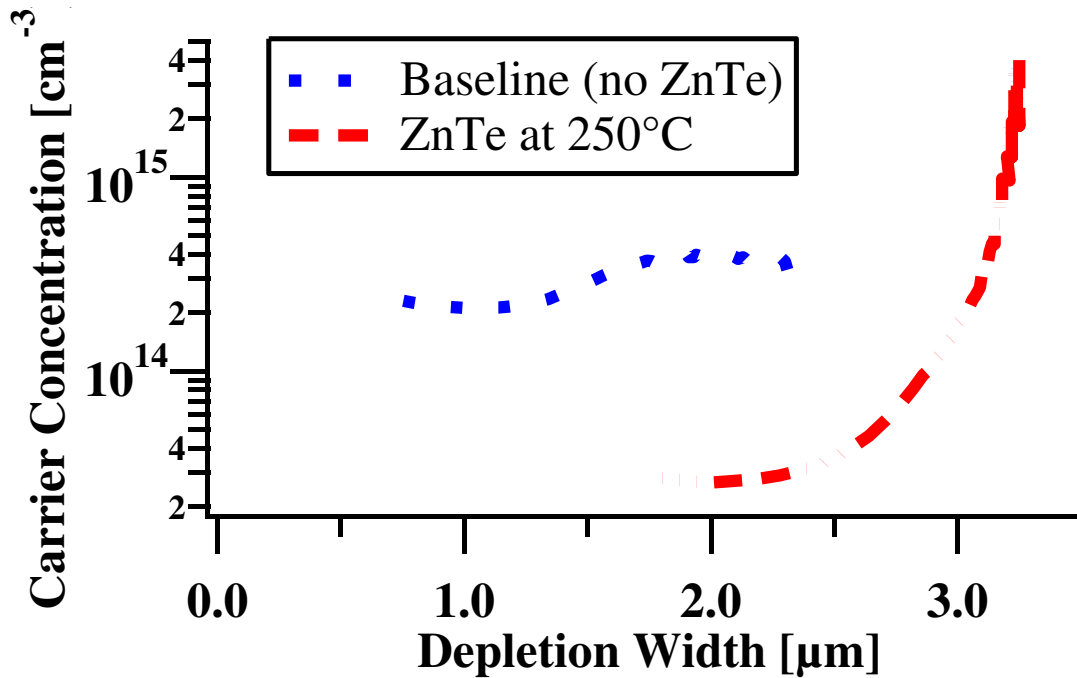
Figure 30: C-V measurements for the best performing ZnTe device and the baseline sample.

From the C-V measurements, the ZnTe device was not completely doped. This indicator led to the exploration of longer copper doping and annealing studies.

Photo Luminescence (PL)

The PL for the final devices were measured and compared. All measurements were performed after the devices were painted. There appeared to be a trend with ZnTe deposition temperature and PL intensity. The lower the ZnTe deposition temperature, the higher the PL signal was. The lowest PL signal in Figure 31 was the ZnTe deposited at 350°C.
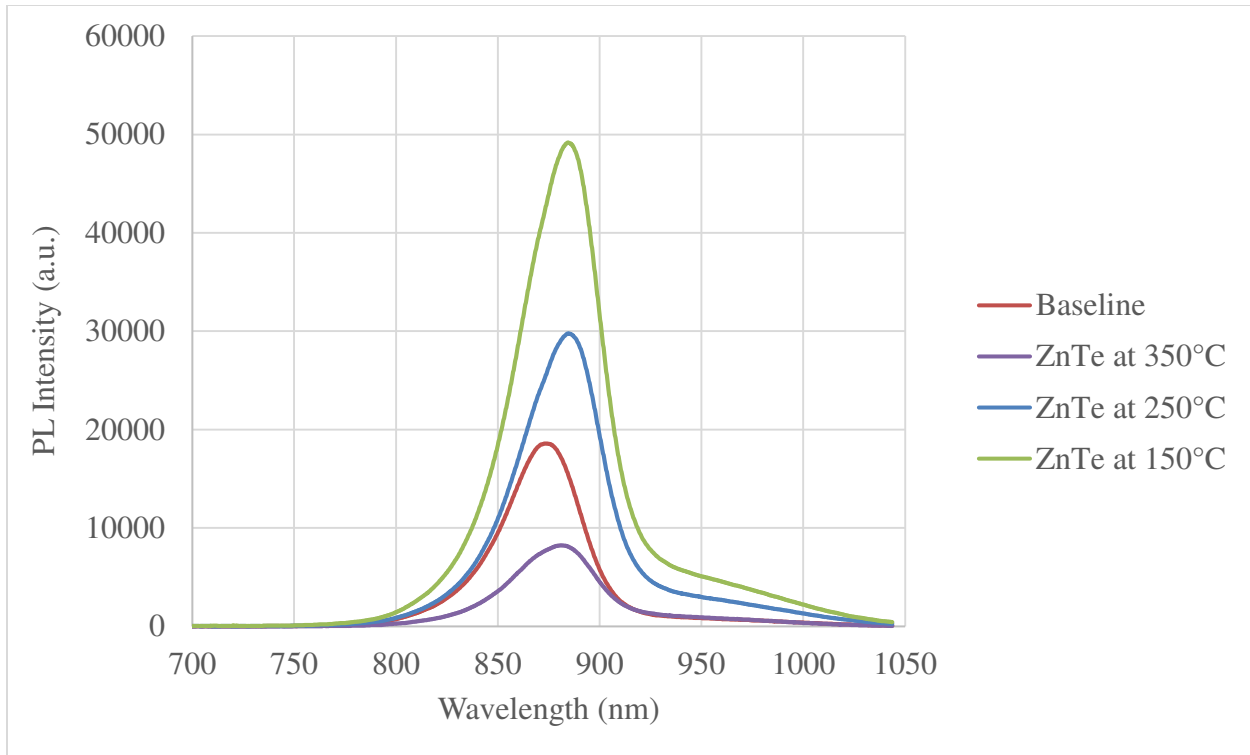
Figure 31: PL intensity for the ZnTe devices and the baseline devices after paint.

4.3.2.2 Impact of Copper doping on ZnTe

Longer copper doping treatments were explored to dope the devices with ZnTe. The copper preheat temperatures were 330°C, the copper chloride temperatures were 190°C, and the annealing temperatures were 200°C. The only variations that occurred with the copper treatments were regarding the time in each source as seen in Table 5.

Table 5: Copper doping treatment recipe times.

Recipe	Preheat	CuCl	Anneal
Standard Copper Treatment	85 s	140 s	280 s
Longer Copper Treatment	120 s	280 s	560 s

J-V Light Testing

The J-V results for the longer copper doping significantly improved the ZnTe device performance as seen in Figure 32. Device performance with and without copper doping on

baseline and ZnTe devices are shown. The devices without intentional copper (solid lines) were very poor performing. The J_{SC} and V_{OC} were very low on the baseline device without copper, however the fill factor was decently high. The ZnTe device without copper had a very poor device performance in all areas. The devices with copper for the ZnTe and baseline case were very good devices with nearly identical efficiencies due to fill factor, J_{SC} and V_{OC}. The longer copper treated device results are displayed in Table 6.
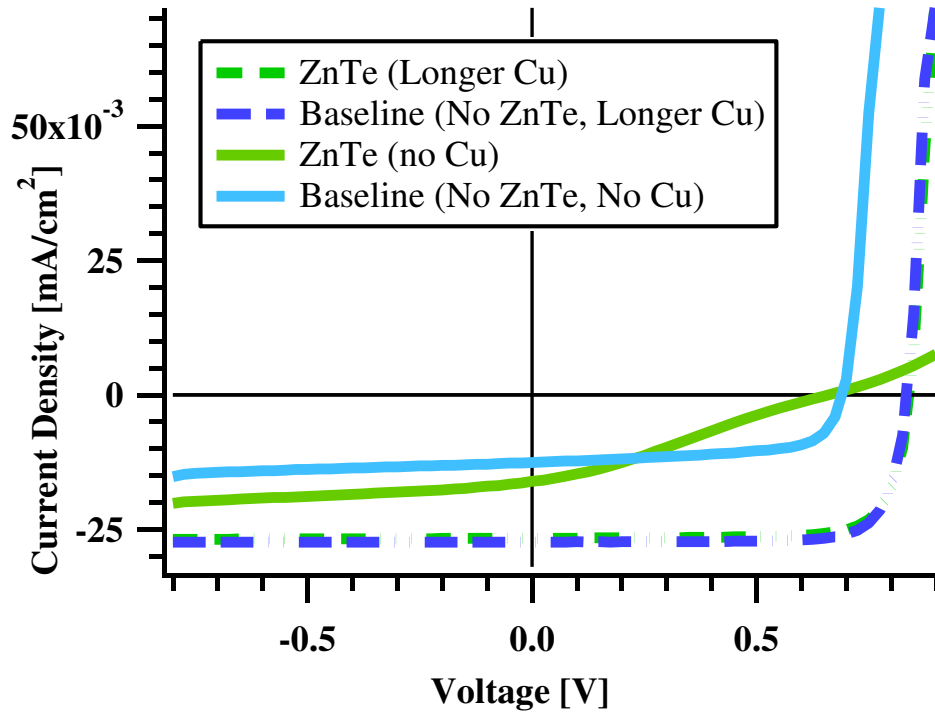
Figure 32: J-V curves for the best devices on each plate.

Table 6: Best performing Devices with the longer copper doping treatment.

Longer Copper Treated Devices	Fill Factor (%)	Jsc (mA/cm^2)	Voc (mV)	Efficiency (%)
Baseline: Cu with Te	79.7	27.4	836	18.24
ZnTe :Cu	78.7	26.7	841	17.66

C-V Testing

The results for the C-V testing show that the doping for the ZnTe device was more uniform throughout. The two devices (baseline and ZnTe) without intentional copper doping had very low carrier concentrations as compared to the longer copper treated devices.
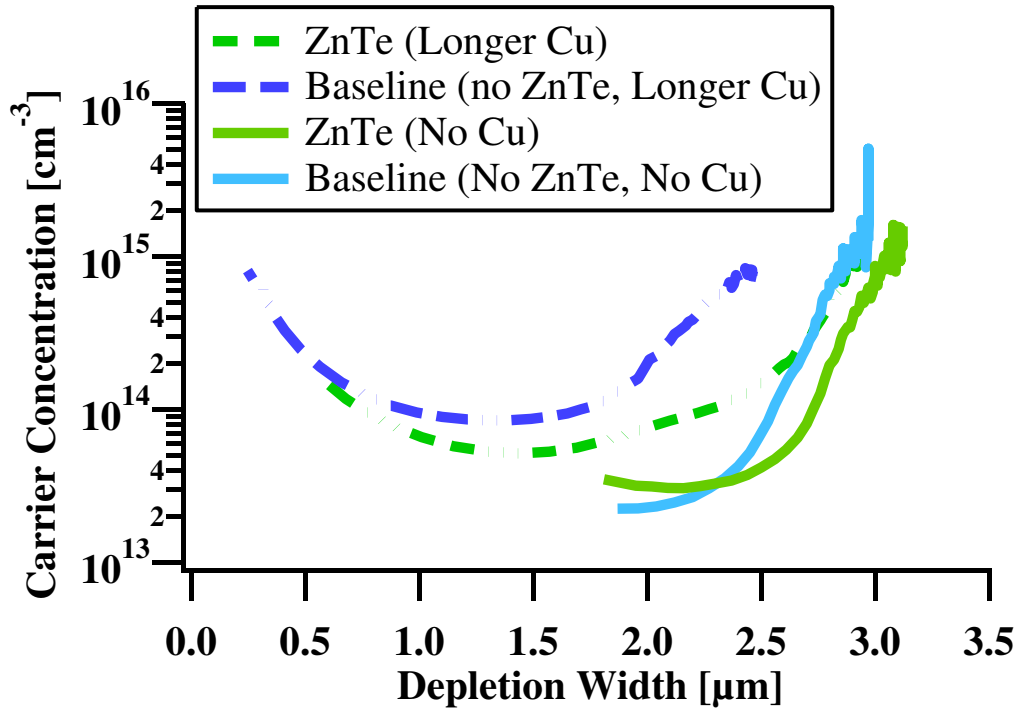
Figure 33: CV performance for baseline and ZnTe devices with and without copper doping.

Photo Luminescence (PL)

There was an interesting observation in the PL signal in Figure 34. The signal intensity was nearly identical for the ZnTe device with and without copper doping. The signal intensity for the baseline device after copper doping dropped significantly as compared to the no intentional copper doping device.
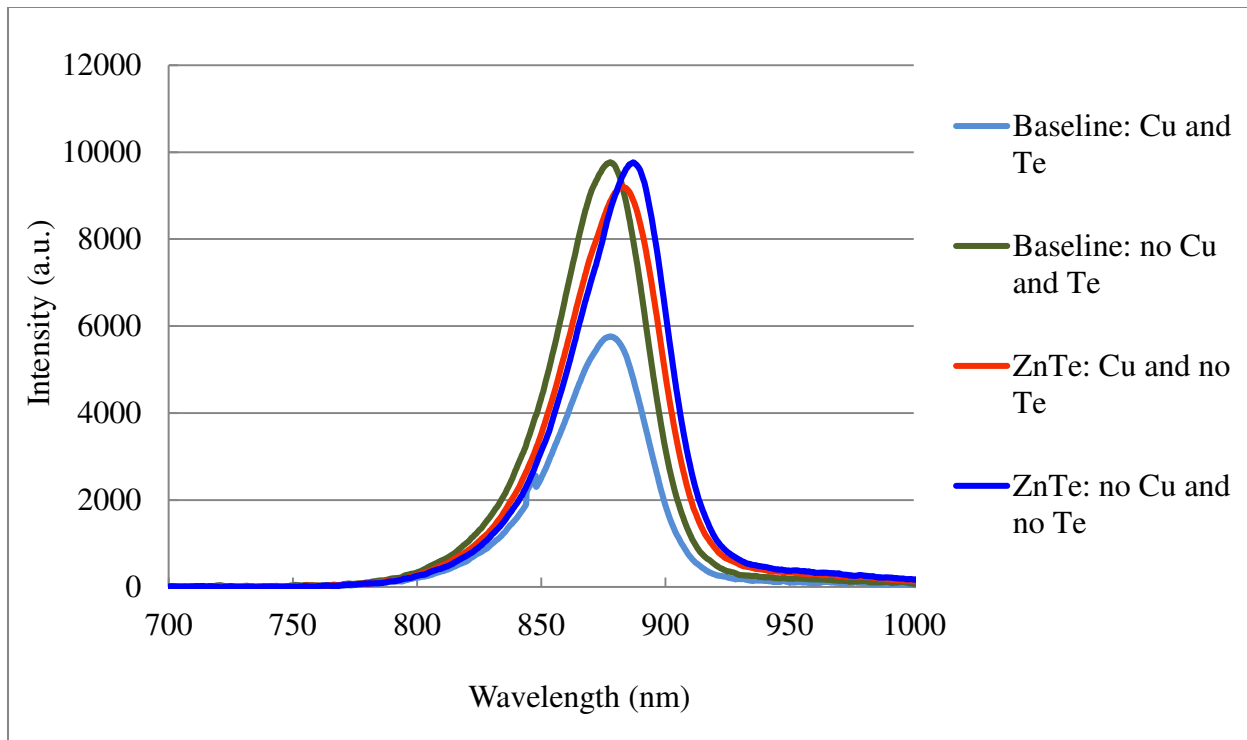
Figure 34: PL signals after each stage of processing for the ZnTe sample and baseline sample with and without intentional copper doping.

5   STABILITY STUDY

5.1 Introduction

Many solar modules now advertise a warranty of 25 years or longer. To prove that the modules will make it in the field for 25 years, accelerated lifetime testing must be performed. For module stability testing, there are three major stressors for solar modules that are considered industry standard. The first test is the damp heat test which is performed at 85% relative humidity and 85°C for 1000 hours or six weeks. The second major test is thermal cycling from -40°C to 85°C where each cycle is a maximum of six hours long for 200 cycles. The third test is the humidity freeze test which is stressed at 85% relative humidity at 85°C for a minimum of 20 hours and then stressed under no relative humidity at -40°C. The humidity freeze test is then performed for 10 cycles [22].

In general, CdTe thin film modules have been reported to degrade over time. However, in CdTe modules the power degradation per year has been found to be lower than those of silicon modules [60]. The average system degradation rate for CdTe modules was found to be 0.6%/ year [61].

5.1.1   CdTe research device performance

"Stress" tests in CdTe cells are often performed at higher temperatures (60-110°C) over an extended time period. Having a stable solar cell is critical not only for the cost effectiveness, but for space applications where solar panels must withstand high energy particles [62].

With stress testing in CdTe solar, there are issues and concerns associated with overall performance. CdTe solar cells with a copper doped back contact tend to show device degradation over time. As the copper diffuses into the device, it causes shunting [62]. A decrease in cell fill factor is often observed followed by a drop in V_{OC}. Often the J_{SC} is not impacted except in

extreme cases [63]. Device stability has been linked to back contact issues and impurities of source material and processes [62].

5.2 Testing Over Time

Devices fabricated at CSU were J-V tested over a period of several weeks. These tests included a baseline and ZnTe device with the longer copper treatment. Devices were stored in a desiccant box at room temperature. The J-V lamp warmed up for at least 40 minutes before the lamp was calibrated. The samples were then tested and compared. Device testing was done as consistently from day to day as possible. Variations in current were observed due to lamp nonuniformities and calibration sample concerns. These variations were observed near the end of sample testing. Results are displayed at the end of the chapter in Figure 35. The ZnTe device had a more consistent fill factor with little variation as compared to the baseline device. The overall efficiencies of the devices are displayed in Figure 36. The large variation seen in the ZnTe device is primarily due to the measured J_{SC} across the plate. The current was not uniform and was lower on one side and increased across the plate. This non-uniformity was attributed to the ZnTe deposition. The baseline device did not have the large variation in current across the device. From the results over time, indicators show that the ZnTe devices were more stable. In order to definitively conclude the device performance, stability testing should be performed in controlled test conditions.
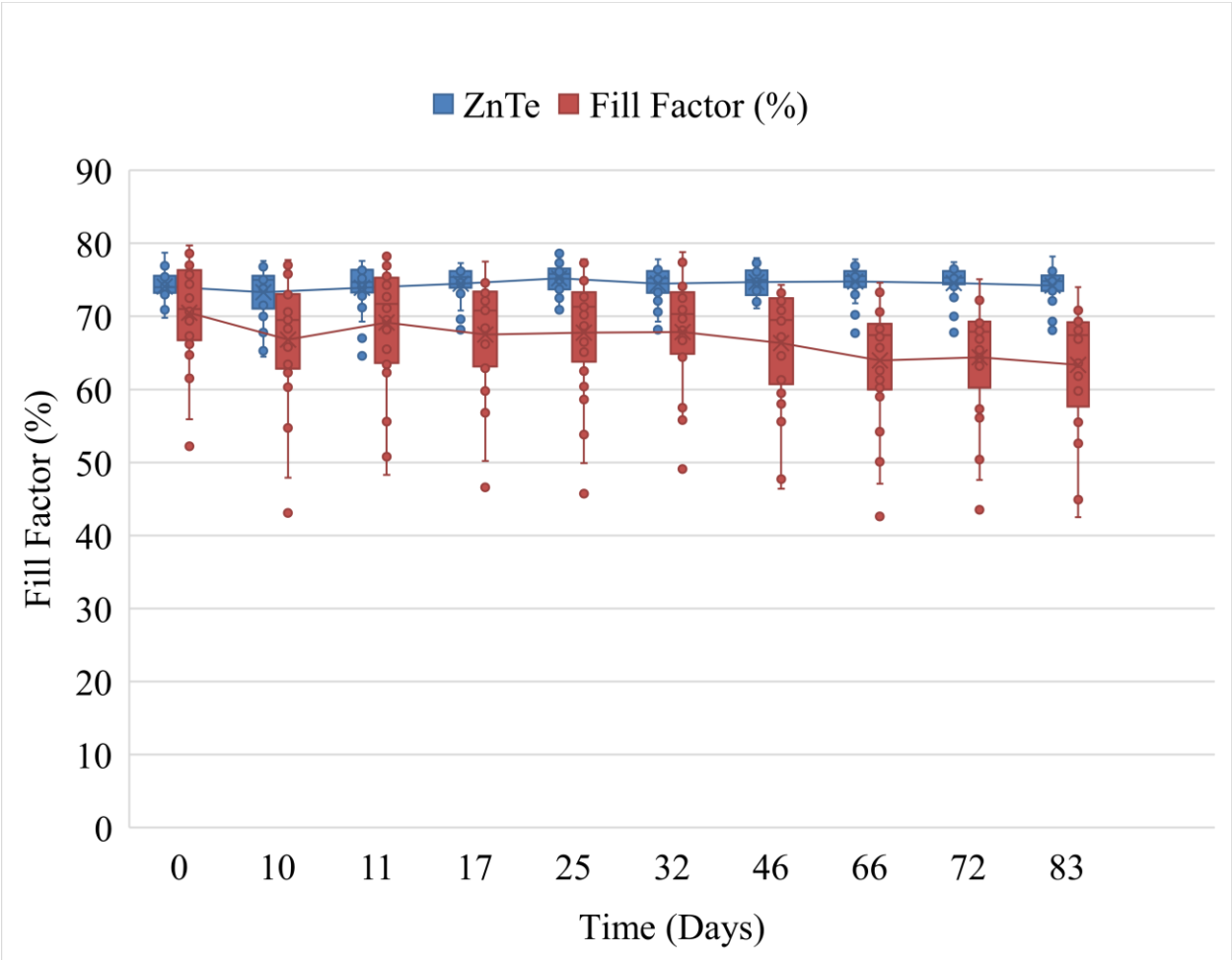
Figure 35: Baseline and ZnTe device fill factor over time.
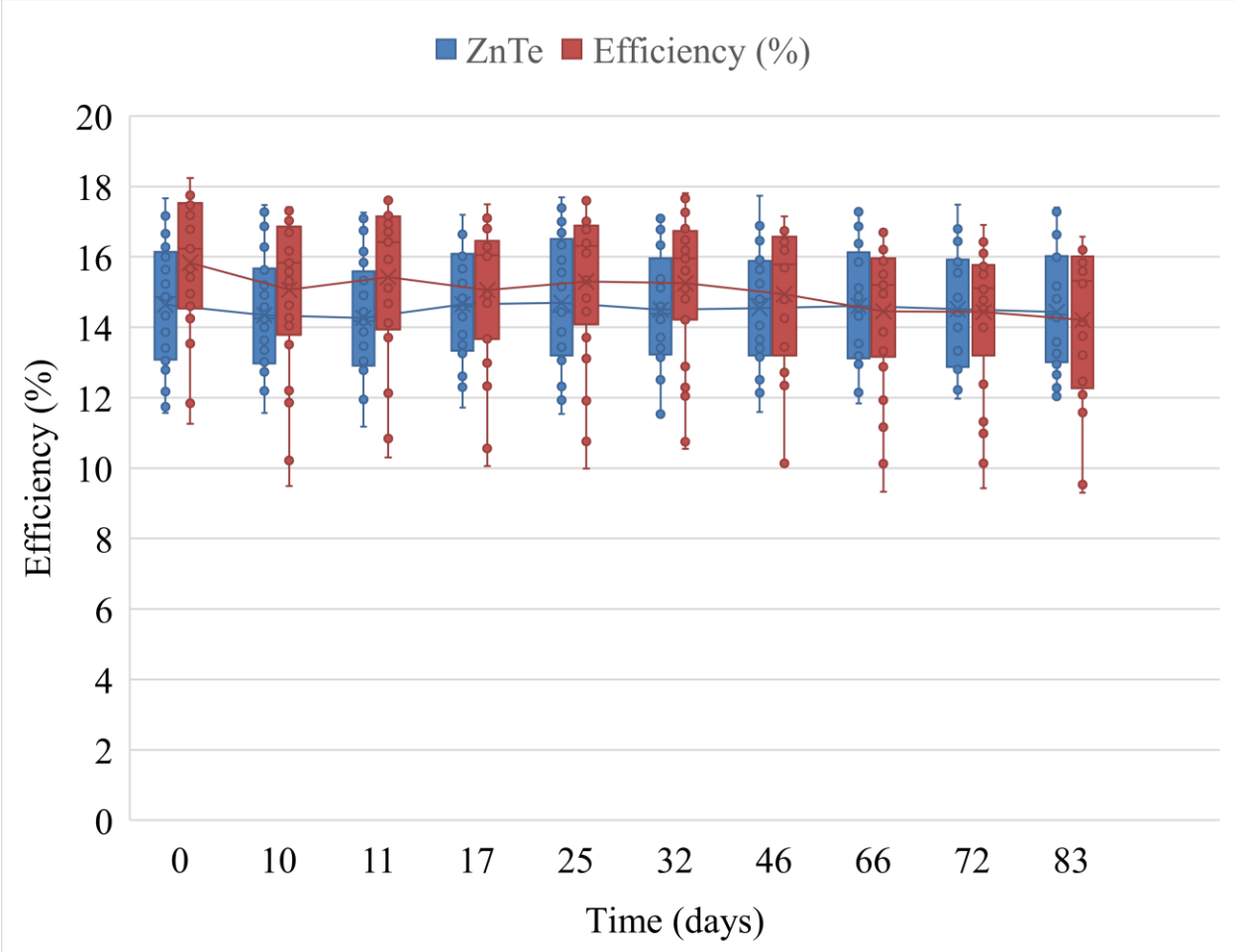
Figure 36: ZnTe and baseline device efficiency over time.

6   CONCLUSIONS

6.1 Summary of Results

This research covered material characterization and device performance of molybdenum, molybdenum oxide, and molybdenum nitride thin films. Film resistivities in general were low as compared to literature values. XPS showed a complex mixture of binding energies, however it did indicate nitrogen and oxygen incorporation into the films. GIXRD reflected crystalline structures for the MoN_x films and amorphous-like for the MoO_x films. Hall measurements indicated carrier mobility increased with increasing oxygen contents, but mobility decreased with increasing nitrogen contents.

As for device performance, the most uniform devices in terms of V_{OC} and fill factor were the 40% N_2/Ar molybdenum back contact with an aluminum back electrode. Results indicated that increasing MoN_x thickness resulted more uniform device performance. A thin layer of tellurium before the molybdenum layers only improved device performance further. Devices with MoN_x were comparable to the baseline device with nickel paint.

Exploring ZnTe as a back contact led to interesting results. The temperature sweep helped discover a better ZnTe deposition temperature of 250°C and the need for a longer copper doping treatment. Device performance with the longer copper doping treatment was comparable with the baseline device.

6.2 Future Work

There are many routes for future work. One option is to further explore the thickness of the ZnTe by doing a large thickness sweep. Much of this work was done referencing Tim Gessert's research with ZnTe: Cu. His ZnTe films were often used as a back contact ranging in thicknesses from 200 nm to over 1000 nm [53].

There are also possibilities to further explore ZnTe: Cu with a MoN_x/ Al capping layer to determine if device performance would still be comparable to the baseline. Future research should also explore 1000-hour stability tests under light and high temperatures up to 100°C. This study would determine the longevity of device performance and potential concerns for degradation.

REFERENCES

[1]   I. C. Conn, "Energy , Transport and the Environment : Providing Energy Security."

[2]   M. Perez and R. Perez, "Update 2015 -- A fundamental look at the supply side energy reserves for the planet," *Nat. Gas*, vol. 2, no. 9, p. 215, 2015.

[3]   I. E. Agency, "Renewables Information 2018: Overview," *IEA Stat.*, p. 497, 2018.

[4]   T. Mai *et al.*, "Renewable Electricity Futures for the United States," *IEEE Trans. Sustain. Energy*, vol. 5, no. 2, pp. 372–378, 2014.

[5]   D. C. Jordan and S. R. Kurtz, "Photovoltaic degradation rates - An Analytical Review," *Prog. Photovoltaics Res. Appl.*, vol. 21, no. 1, pp. 12–29, 2013.

[6]   H. Z. Ã *et al.*, "The history of solar," *Sol. Energy Mater. Sol. Cells*, vol. 93, pp. 1461– 1470, 2011.

[7]   International Renewable Energy Agency (IRENA), *IRENA (2018), Renewable capacity statistics 2018*. 2018.

[8]   R. Fu, D. Feldman, R. Margolis, R. Fu, D. Feldman, and R. Margolis, "U . S . Solar Photovoltaic System Cost Benchmark : Q1 2018 U . S . Solar Photovoltaic System Cost Benchmark : Q1 2018," no. November, 2018.

[9]   P. Hersch and K. Zweibel, *Basic Photovoltaic Principles and Methods*. Office, U S Government Printing Technical, National Service, Information, 1982.

[10]   M. A. Green, *Solar Cells. Operating Principles, Technology, and Systems Applications*. Prentice-Hall Series in Solid State Physical Electronics, 1982.

[11]   "Energy 101: Solar PV." [Online]. Available: https://www.energy.gov/eere/videos/energy-101-solar-pv.

[12]   Pearsonhighered, "N-Type and P-Type Semiconductors," *Introd. to Semicond.*, pp. 1–13, 2013.

[13]   "Semiconductor devices," *Springer Ser. Mater. Sci.*, vol. 207, pp. 195–233, 2014.

[14]   S. A. Al Kuhaimi, "Conduction and valence band offsets of CdS/CdTe solar cells," *Energy*, vol. 25, no. 8, pp. 731–739, 2000.

[15]   A. Kahn, "Fermi level, work function and vacuum level," *Mater. Horizons*, vol. 3, no. 1, pp. 7–10, 2016.

[16]   "P-Type, N-Type Semiconductors," *Libretexts Engineering*, 2019. [Online]. Available: https://eng.libretexts.org/Bookshelves/Materials_Science/Supplemental_Modules_(Materials_Science)/The_Science_of_Solar/Solar_Basics/D._P-N_Junction_Diodes/I._P-Type%2C_N-Type_Semiconductors.

[17]   NASA, "Terrestrial Photovoltaic Measurement Procedures," *ENERGY Res. Off. Assist. Adm. Dev. Adm. Solar, Geothermal, Adv. Energy Syst. Div. Sol. Energy*, p. 11, 1977.

[18]   "Reference Air Mass 1.5 Spectra." [Online]. Available: NREL.gov/grid/solar-resource/spectra-am1.5.html. [Accessed: 27-Jul-2019].

[19]   "First Solar Q3' 13 Earnings Call," 2013.

[20]   W. Shockley and H. J. Queisser, "Detailed balance limit of efficiency of p-n junction solar cells," *J. Appl. Phys.*, vol. 32, no. 3, pp. 510–519, 1961.

[21]   G. M. Albuquerque, "Theoretical limit for efficiency of silicon solar cells 'The Shockley-Queisser Limit and Beyond,'" 2019.

[22]   N. Strevel, L. Trippel, C. Kotarba, and I. Khan, "Improvements in CdTe module reliability and long-term degradation through advances in construction and device innovation," *Photovoltaics Int.*, pp. 1–8, 2013.

[23]   "Best Research-Cell Efficiency Chart," 2019. [Online]. Available:

        https://www.nrel.gov/pv/cell-efficiency.html.

[24]   J. M. Kephart, "OPTIMIZATION OF THE FRONT CONTACT TO MINIMIZE SHORT-

        CIRCUIT CURRENT LOSSES IN CDTE THIN-FILM SOLAR CELLS," 2015.

[25]   D. E. Swanson *et al.*, "Single vacuum chamber with multiple close space sublimation

        sources to fabricate CdTe solar cells," *J. Vac. Sci. Technol. A Vacuum, Surfaces, Film.*,

        vol. 34, no. 2, p. 021202, 2016.

[26]   S. Uličná, P. J. M. Isherwood, P. M. Kaminski, J. M. Walls, J. Li, and C. A. Wolden,

        "Development of ZnTe as a back contact material for thin film cadmium telluride solar

        cells," *Vacuum*, vol. 139, pp. 159–163, 2017.

[27]   "Four Point Probe Resistivity Measurements," *Pveducation*. [Online]. Available:

        https://www.pveducation.org/pvcdrom/characterisation/four-point-probe-resistivity-

        measurements.

[28]   E. Ramsden, *Hall-Effect Sensors Theory and Applications*, Second., no. I. Elsevier, 2006.

[29]   D. Abou-Ras, T. Kirchhartz, and U. Rau, *Advanced Characterization Techniques for Thin

        Film Solar Cells*. 2011.

[30]   F. Sima, C. Ristoscu, L. Duta, O. Gallet, K. Anselme, and I. N. Mihailescu, "Laser thin

        films deposition and characterization for biomedical applications," in *Laser Surface

        Modification of Biomaterials: Techniques and Applications*, 2016.

[31]   S. S. Hegedus and W. N. Shafarman, "Thin-film solar cells: device measurements and

        analysis," *Prog. Photovoltaics Res. Appl.*, vol. 12, no. 23, pp. 155–176, 2004.

[32]   J. V. Li *et al.*, "Theoretical analysis of effects of deep level, back contact, and absorber

        thickness on capacitance-voltage profiling of CdTe thin-film solar cells," *Sol. Energy*

Mater. Sol. Cells, vol. 100, pp. 126–131, 2012.

[33] "Electrical Characterization of Photovoltaic Materials and Solar Cells with the 4200A-SCS Parameter Analyzer." .

[34] K. K. Smith, "Photoluminescence of semiconductor materials," *Thin Solid Films*, vol. 84, no. 2, pp. 171–182, 1981.

[35] S. Swann, "Magnetron sputtering," *Phys. Technol.*, pp. 67–75, 1988.

[36] M. Hughes, "What is sputtering? Magnetron sputtering?," *The Global Source Semicore*, 2014. .

[37] H. B. Michaelson, "Work functions of the elements," *J. Appl. Phys.*, 1977.

[38] R. Yang, D. Wang, M. Jeng, K. Ho, and D. Wang, "Stable CdTe thin film solar cells with a MoOxback-contact buffer layer.pdf," *Prog. Photovoltaics Res. Appl.*, vol. 24, pp. 59–65, 2016.

[39] H. Lin, Irfan, W. Xia, H. N. Wu, Y. Gao, and C. W. Tang, "MoO x back contact for CdS/CdTe thin film solar cells: Preparation, device characteristics, and stability," *Sol. Energy Mater. Sol. Cells*, vol. 99, pp. 349–355, 2012.

[40] N. R. Paudel, A. D. Compaan, and Y. Yan, "Sputtered CdS/CdTe solar cells with MoO3-x/Au back contacts," *Sol. Energy Mater. Sol. Cells*, vol. 113, pp. 26–30, 2013.

[41] S.-Y. Lin and Y.-S. Lai, "Effect of Nitrogen on the Physical Properties and Work Function of MoNx Cap Layers on HfO2 Gate Dielectrics," *ECS J. Solid State Sci. Technol.*, vol. 3, no. 12, pp. N161–N165, 2014.

[42] R. E. Cuthrell, D. M. Mattox, C. R. Peeples, P. L. Dreike, and K. P. Lamppa, "Residual stress anisotropy, stress control, and resistivity in post cathode magnetron sputter deposited molybdenum films," *J. Vac. Sci. Technol. A Vacuum, Surfaces, Film.*, vol. 6, no.

5, pp. 2914–2920, 1988.

[43]   A. E.-H. B. Kashyout, H. M. A. Soliman, H. A. Gabal, P. A. Ibrahim, and M. Fathy, "Preparation and characterization of DC sputtered molybdenum thin films," *Alexandria Eng. J.*, vol. 50, no. 1, pp. 57–63, Mar. 2011.

[44]   I. Jauberteau *et al.*, "Molybdenum Nitride Films: Crystal Structures, Synthesis, Mechanical, Electrical and Some Other Properties," *Coatings*, vol. 5, no. 4, pp. 656–687, 2015.

[45]   J. Musil, P. Baroch, J. Vlček, K. H. Nam, and J. G. Han, "Reactive magnetron sputtering of thin films: Present status and trends," *Thin Solid Films*, vol. 475, no. 1-2 SPEC. ISS., pp. 208–218, 2005.

[46]   I. Safi, "Recent aspects concerning DC reactive magnetron sputtering of thin films: a review," *Surf. Coatings Technol.*, vol. 127, pp. 203–219, 2000.

[47]   C. Gretener *et al.*, "Development of MoOx thin films as back contact buffer for CdTe solar cells in substrate configuration," *Thin Solid Films*, vol. 535, no. 1, pp. 193–197, 2013.

[48]   X. Liu, S. Yi, C. Wang, I. Irfan, and Y. Gao, "Effect of oxygen plasma treatment on air exposed MoOx thin film," *Org. Electron. physics, Mater. Appl.*, vol. 15, no. 5, pp. 977–983, 2014.

[49]   "Table 1-1. Electron binding energies, in electron volts, for the elements in their natural forms.," p. 2013, 2013.

[50]   B. Brox and I. Olefjord, "ESCA Studies of MoO2 and MoO3," *Surf. Interface Anal.*, vol. 13, no. 1, pp. 3–6, 1988.

[51]   J. G. Choi and L. T. Thompson, "XPS study of as-prepared and reduced molybdenum

oxides," *Appl. Surf. Sci.*, vol. 93, no. 2, pp. 143–149, 1996.

[52] I. Takano, S. Isobe, T. A. Sasaki, and Y. Baba, "Nitrogenation of various transition metals by N+2-ion implantation," *Appl. Surf. Sci.*, vol. 37, no. 1, pp. 25–32, 1989.

[53] T. A. Gessert, W. K. Metzger, P. Dippo, S. E. Asher, R. G. Dhere, and M. R. Young, "Dependence of carrier lifetime on Cu-contacting temperature and ZnTe:Cu thickness in CdS/CdTe thin film solar cells," *Thin Solid Films*, vol. 517, no. 7, pp. 2370–2373, 2009.

[54] M. D. Kempe, "Control of moisture ingress into photovoltaic modules," in *31st IEEE Photovoltaics Specialists Conference and Exhibition*, 2005, pp. 1–4.

[55] D. Rioux, D. W. Niles, and H. Höchst, "ZnTe: A potential interlayer to form low resistance back contacts in CdS/CdTe solar cells," *J. Appl. Phys.*, vol. 73, no. 12, pp. 8381–8385, 1993.

[56] First Solar, "First Solar ® FS Series 3 ™ Black PV Module," vol. 1, no. January, pp. 4–5, 2014.

[57] D. Cahen, K. Gartsman, G. Hodes, O. Rotlevy, and K. Dobson, "Overcoming Degradation Mechanisms in CdTe Solar Cells Overcoming Degradation Mechanisms in CdTe Solar Cells First Annual Report," no. February, 2000.

[58] C. Narayanswamy, T. A. Gessert, and S. E. Asher, "Analysis of Cu diffusion in ZnTe-based contacts for thin-film CdS/CdTe solar cells," vol. 248, no. 1999, pp. 248–253, 1999.

[59] T. A. Gessert, X. Li, T. J. Coutts, A. R. Mason, and R. J. Matson, "Dependence of material properties of radio-frequency magnetron-sputtered, Cu-doped, ZnTe thin films on deposition conditions," *J. Vac. Sci. Technol. A*, vol. 12, no. 4, pt.1, pp. 1501–1506, 1994.

[60] R. Dubey *et al.*, "Comprehensive study of performance degradation of field-mounted photovoltaic modules in India," *Energy Sci. Eng.*, vol. 5, no. 1, pp. 51–64, 2017.

[61] B. Marion, J. A. del Cueto, P. McNutt, and D. Rose, "Performance Summary for the First Solar CdTe 1 kW System," no. October, pp. 1–4, 2001.

[62] D. L. Bätzner, A. Romeo, M. Terheggen, M. Döbeli, H. Zogg, and A. N. Tiwari, "Stability aspects in CdTe/CdS solar cells," in *Thin Solid Films*, 2004.

[63] B. E. McCandless and J. R. Sites, "Chapter 14: Cadmium Telluride Solar Cells," in *Handbook of Photovoltaic Science and Engineering*, John Wiley and Sons, 2011, pp. 600–641.

PUBLICATIONS AND CONFERENCE PROCEEDINGS

1. **Kindvall**, A.H. Munshi, T. Shimpi, A.H. Danielson, and W.S. Sampath, "Effect of Process Temperature and Copper Doping on the Performance of ZnTe:Cu Back Contacts in CdTe Photovoltaics," 46th IEEE Photovoltaic Specialists Conference, 2019.

2. Danielson, A. Munshi, A. Onno, W. Weigand, **A. Kindvall**, C. Reich, Z.J. Yu, J. Shi, D. Kuciauskas, A. Abbas, J. Walls, Z. Holman, W. Sampath, "Sputtered Aluminum Oxide and p^+ Amorphous Silicon Back-Contact for Improved Hole Extraction Polycrystalline $CdSe_xTe_{1-x}$ and CdTe Photovoltaics," 46th IEEE Photovoltaic Specialists Conference, 2019.

3. **A. Kindvall**, A.H. Munshi, T. Shimpi, A.H. Danielson, and W.S. Sampath, "Copper Doped Zinc Telluride Thin-Films as a Back Contact for Cadmium Telluride Photovoltaics," 45th IEEE Photovoltaic Specialists Conference, 2018.

4. T. Shimpi, D. Swanson, C. Reich, J.M. Kephart, **A. Kindvall**, R. Pandey, Z. Holman, K.L. Barth, and W. S. Sampath, "Co-Sublimated Polycrystalline Cd1-xZnxTe Films for Multi-junction Solar Cells," 45th IEEE Photovoltaic Specialists Conference, 2018.

5. A.H. Munshi, A. H. Danielson, **A. Kindvall**, K. L. Barth, and W. S. Sampath, "Investigation of Sputtered Oxides and p+ Back-contact for Polycrystalline CdTe and CdSeTe Photovoltaics," 45th IEEE Photovoltaic Specialists Conference, 2018.

6. A.H. Danielson, A.H. Munshi, **A. Kindvall**, S.K. Swain, K.L. Barth, K. Lynn, and W.S. Sampath. "Doping CdTe Absorber Cells using Group V Elements," 45th IEEE Photovoltaic Specialists Conference, 2018.

7. J.M.Kephart, **A. Kindvall**, D. Williams, D. Kuciauskas, P. Dippo, A. Munshi, W.S. Sampath, "Sputter-Deposited Oxides for Interface Passivation of CdTe Photovoltaics," *IEEE Journal of Photovoltaics*, vol. 8, no. 2, pp. 587-593, Mar. 2018

8. **A. Kindvall**, J. M. Kephart, W.S. Sampath, "Molybdenum Oxide and Molybdenum Nitride Back Contacts for Thin Film CdTe Solar Cells," *44th IEEE Photovoltaic Specialists Conference*, June 2017.